The Sicily Channel surface circulation revisited using a neural clustering analysis of a high-resolution simulation

Manel Jouini, Karine Béranger, Thomas Arsouze, Jonathan Beuvier, Sylvie Thiria, Michel Crépon, Isabelle Taupier-Letage

The Sicily Channel surface circulation revisited using a neural clustering analysis of a high-resolution simulation

Manel Jouini[1], Karine Béranger[2,3,4], Thomas Arsouze[2,3], Jonathan Beuvier[5,6],

Sylvie Thiria[1], Michel Crépon[1], and Isabelle Taupier-Letage[7]

Corresponding author: K. Béranger, Laboratoire d'étude des Transferts en Hydrologie et Environnement, UMR5564, Domaine Universitaire, Bâtiment A-BERGES ENSE3, 1025 Rue de la piscine, 38000 Saint-Martin d'Hères, France. (karine.beranger@ujf-grenoble.fr)

[1]LOCEAN, Tour 45-55, Boite 100, 4 Place Jussieu, 75252 Paris Cedex 05, France.

[2]LMD, Ecole Polytechnique, 91128 Palaiseau Cedex, France

[3]ENSTA-ParisTech, Université Paris-Saclay, 828 Boulevard des Maréchaux, 91762 Palaiseau Cedex, France.

[4]LTHE, UMR5564, OSUG-B, BP 53, 38041 Grenoble Cedex 9, France.

[5]Mercator Ocean, 8-10 Rue Hermès, Parc Technologique du Canal, 31520 Ramonville St-Agne, France.

[6]Météo-France, 42, avenue Gaspard Coriolis, 31057 Toulouse Cedex, France.

[7]MIO, Antenne de La Seyne, CS 20330, 83507 La Seyne, France.

Contents of this file

Abstract

The Sicily Channel surface circulation is investigated by analyzing the outputs of a high-resolution ocean model MED12 forced during 46 years by the ARPERA atmospheric fields. Applying a neural network classifier, we show that the surface circulation in the Sicily Channel can be decomposed into 8 modes characterizing the major patterns of that circulation, particularly the Algerian Current separation at the entrance to the Sicily Channel, the features of the Atlantic Tunisian Current and of the Atlantic Ionian Stream. These modes reflect the variability of the circulation in space and time at seasonal and inter-annual scales. Some modes preferably occur in winter whilst others are characteristic of summer. The mode sequence presents an inter-annual variability in good agreement with observations. The topography of the Sicily Channel sill plays a major role in steering the circulation. In particular the summer upwelling along the southern coast of Sicily, which is present in several modes, could be explained by a large-scale density forcing. A combination of barotropic/baroclinic double Kelvin waves generated on both sides of the sill provides a mechanism for explaining the complexity of the surface circulation advecting the surface waters from the Western Mediterranean towards the Eastern Mediterranean, the most salient features of which are the Atlantic Tunisian Current, the Atlantic Ionian Stream and the Tyrrhenian Sicilian Current which is a new feature highlighted by the present study.

Key words: Sicily Channel, Circulation Variability, Neural Clustering.

1. Introduction

The Sicily Channel (SC here-after), which is characterized by a sill of about 400 m depth, controls the water exchanges between the Western Mediterranean and the Eastern Mediterranean, and thus plays a major role in constraining the Mediterranean Sea circulation. The large scale circulation of the Mediterranean Sea is forced by air-sea fluxes of energy and mass, which determine the formation of dense water masses generating a thermohaline circulation [*Lacombe et al.*, 1985; *Béthoux and Tailliez*, 1994; *Béthoux and Gentili*, 1999; *Millot and Taupier-Letage*, 2005]. The circulation in the SC can be described as a two-layer exchange of inflowing low-density water in the top layer, and of outflowing higher-density water in the bottom layer. The low-density water coming from the Western Mediterranean occupies the top 150 m surface layer and is mainly composed of Atlantic Water (AW). The higher-density water coming from the Eastern Mediterranean occupies the 150-400 m depth zone and is mainly composed of water circulating at intermediate depths in the Eastern Mediterranean, in particular the Levantine Intermediate Water (LIW). The transport of these two main flows is highly variable at seasonal and inter-annual scales [*Astraldi et al.*, 2002; *Béranger et al.*, 2005].

The circulation of the surface layer in the SC has been synthesized from the data of many oceanographic campaigns and by modelling studies; it can be schematized as follows (Figure 1, Table 1). The Algerian Current (AC) advects the AW eastwards along the Algerian slope and splits into two branches at the entrance to the SC, owing to a topographic effect caused by the Sicily sill [*Herbaut et al.*, 1998]. A first branch of the AW stream penetrates into the Tyrrhenian Sea forming the Bifurcation Tyrrhenian Current

(BTC, as denoted by *Sorgente et al.* [2011]), which flows along the northern coast of Sicily, while the second branch crosses the SC and enters the Eastern Mediterranean running along the coast of Tunisia [*Manzella et al.*, 1990] forming the Atlantic Tunisian Current (ATC, as denoted by *Béranger et al.* [2004]). In several high-resolution models, the BTC generally flows eastwards along the northern coast of Sicily [*Onken et al.*, 2003; *Pierini and Rubino*, 2001; *Napolitano et al.*, 2003; *Béranger et al.*, 2004], while in some others [*Pierini and Rubino*, 2001; *Sorgente et al.*, 2003; *Béranger et al.*, 2004], the BTC presents a secondary bifurcation near 11°E flowing north-westwards, which forms a cyclonic circulation denoted as the South Eastern Sardinian Gyre (SESG) by *Sorgente et al.* [2011]. We also observe an additional AW stream entering the Eastern Mediterranean and flowing along the southern coast of Sicily forming the Atlantic Ionian Stream (AIS, as denoted by *Robinson et al.* [1999]).

This description is in agreement with recent observations made with surface drifters released in the SC [*Poulain and Zambianchi*, 2009; *Gerin et al.*, 2009], infra-red remote-sensing studies [*Hamad et al.*, 2006; *Taupier-Letage*, 2008] and very high-horizontal-resolution modelling studies at (1/32°) [*Sorgente et al.*, 2011; *Olita et al.*, 2012] resolving the first radius of deformation of the Mediterranean Sea. It is important to emphasize that very few drifters have been launched at the western entrance to the channel (south of the Tyrrhenian Sea), most of the floats being released in the SC [*Poulain and Zambianchi*, 2009; *Gerin et al.*, 2009]. Consequently, although the circulation at the eastern exit to the SC is well known, it is poorly documented for the western entrance to the SC [*Ben Ismail et al.*, 2012].

Besides, a large part of these studies shows that the circulation in the SC region is subject to seasonal variations, as for example a more pronounced ATC in winter than in summer [*Béranger et al.*, 2004] or the occurrence of an upwelling on the southern coast of Sicily in summer [*Robinson et al.*, 1999; *Lermusiaux and Robinson*, 2001; *Béranger et al.*, 2004]. For the 2009-2011 period, *Sorgente et al.* [2011] using their very high-resolution model, showed several bifurcations of the ATC and of the BTC (Figure 1). The ATC can split near Lampedusa Island and form the Bifurcation Atlantic Tunisian Current (BATC) or the Atlantic Libyan Current (ALC). And in summer, they demonstrated the presence of the Westward Northern Sicilian Current (WNSC) in the Tyrrhenian Sea. But these descriptions are still controversial, owing to the presence of important mesoscale structures like eddies or plumes [*Sammari et al.*, 1999; *Lermusiaux*, 1999; *Ciappa*, 2009] (see the Figure 1 in *Sorgente et al.* [2011], for a review) which may have an impact on a large part of the AW transport [*Onken et al.*, 2003; *Napolitano et al.*, 2003; *Fernandez et al.*, 2005; *Ben Ismail et al.*, 2012]. *Molcard et al.* [2002] argued that the mean paths of AW are not sensitive to the magnitude of the density gradient between the Western Mediterranean and the Eastern Mediterranean, but a modulation of the paths of the different bifurcation branches was found in the sensitivity experiments of *Pierini and Rubino* [2001] and in the seasonal analysis of *Vetrano et al.* [2004] based on an inverse model applied to *in situ* observations. Moreover, *Poulain and Zambianchi* [2009] utilized the wind forcing to explain the seasonal variations of the circulation, while *Pierini and Rubino* [2001] invoked non-linear effects for determining the surface bifurcation process. Recent observations show that these circulation outlines can be modulated at decadal scales by well marked events such as the Eastern Mediterranean Transient in the 1990's

[*Roether et al.*, 2007], the recent deep water renewal called the Western Mediterranean Transition after 2005 [*Schroeder et al.*, 2008], and the Adriatic-Ionian Bimodal Oscillating System (BiOS) evidenced by *Gacic et al.* [2010].

The aim of the present paper is to provide a revised description and interpretation of the AW circulation in the Sicily Channel and to identify the different AW paths and mesoscale patterns by analyzing a 46-year high-resolution simulation of this region forced by realistic atmospheric fluxes and winds. Some major questions arise about the functioning of the Sicily Channel. Is the current regime stable? Can we define specific regimes related to the seasonal or inter-annual variations of the current patterns? What are the possible mechanisms responsible for such regimes? In order to answer these questions, we decided to use a high-performance clustering method to extract, in the statistical sense, the most pertinent channel circulation situations from the multi-decadal numerical simulation of the Mediterranean Sea [*Beuvier et al.*, 2012a]. As done in previous works, with success [*Liu et al.*, 2007; *Mihanovic et al.*, 2011], we computed the different modes of the circulation using a neural network clustering method, the so-called Self Organized Map (SOM) [*Kohonen and Somervuo*, 2002].

The paper is articulated as follows: the numerical model experiment and the clustering methodology for analyzing the model outputs are detailed in Section 2 and Section 3, respectively. The main characteristics of the different circulation regimes are presented in Section 4. The reality of a new branch of the sea-surface circulation is discussed in Section 5 and an explanation of the origin of its generation is investigated using conceptual models. Summary and conclusions are presented in Section 6. Acronyms used in the following can be found in Tables 1 and 2.

2. The MED12 simulation

We use the ocean free-surface general circulation model NEMO [*Madec and The-NEMO-Team*, 2008] in a regional configuration of the Mediterranean Sea called MED12 [*Lebeaupin Brossier et al.*, 2011; *Beuvier et al.*, 2012b] developed in the framework of the national MORCE and SiMED projects. For this study, we use 46 years (1966-2011) of the long-term simulation of *Beuvier et al.* [2012a] forced during the 1958-2013 period by the atmospheric fields of ARPERA [*Herrmann and Somot*, 2008].

The MED12 configuration (see *Beuvier et al.* [2012b] for details) covers the whole Mediterranean Sea plus a buffer zone including a part of the near Atlantic Ocean. The horizontal resolution is about 7 km and we use 50 stretched z-levels on the vertical. A Laplacian operator is applied along iso-neutral surfaces for tracers with a horizontal eddy diffusivity coefficient of 60 $m^2.s^{-1}$ while a biharmonic operator is applied for the momentum with a horizontal viscosity coefficient of -1.25 10^{10} $m^4.s^{-2}$. The TVD (Total Variance Dissipation) scheme is used for the tracer advection and the EEN (Energy and ENstrophy conservative) scheme is used for the momentum advection [*Barnier et al.*, 2006]. The vertical diffusivity for tracers and momentum is modeled with the standard turbulent kinetic energy closure scheme of NEMO [*Blanke and Delecluse*, 1993] with a vertical diffusivity coefficient increased to 10 $m^2.s^{-1}$ in case of vertical static instabilities. A time-step of 12 minutes is used. No-slip conditions are applied at the lateral boundaries, while at the sea bed, a bottom friction is applied taking into account a 2D field of the mean tidal energy computed from the tidal model of *Lyard et al.* [2006].

The initial conditions in the Mediterranean domain are provided by the monthly mean potential temperature and salinity 3D fields from the MEDATLAS-II climatology [*The-*

MEDAR-Group, 2002]. These fields are smoothed by a low-pass filtering with a 10-year time-window using the MEDATLAS data covering the 1955-1965 period. The simulation then starts in October 1958 with an ocean at rest.

In order to represent the inter-annual variability of the exchanges through the Strait of Gibraltar, the Atlantic Ocean is modelled as a buffer zone where the 3D temperature and salinity of MED12 are relaxed towards the climatological fields of *Levitus et al.* [2005] on which the monthly anomalies of the ENSEMBLES global oceanic reanalysis [*Daget et al.*, 2009] are superimposed. And in this buffer zone, the modelled sea-surface height is relaxed to a sea-surface height climatology built from the global ocean reanalyses of *Ferry et al.* [2010].

The river runoff is provided by the monthly climatology of *Ludwig et al.* [2009] and is distributed in the main Mediterranean river mouths and as coastal runoff. The Black Sea freshwater input is applied as a river, using the estimates of *Stanev and Peneva* [2002].

The MED12 model is forced by the daily fields of the momentum, freshwater and heat fluxes of the atmospheric forcing ARPERA, which is a dynamical downscaling of ECMWF products above the European-Mediterranean domain performed with the ARPEGE-Climat model [*Herrmann and Somot*, 2008]. The simulated period extends from 1 October 1958 to 31 December 2013. For the period 1958-2001, the driven fields of ARPERA come from the coarse resolution ERA40 reanalysis [*Simmons and Gibson*, 2000], whereas from 2002 to 2013 the driven fields come from the higher resolution ECMWF analyses [*Richardson*, 2006] after being downgraded to the ERA40 resolution to ensure consistency between the two successive periods. This method has already been evaluated in *Beuvier et al.* [2010]. In the formulation of the surface temperature condition, a relax-

ation of the model sea-surface temperature (SST here-after) is applied to the ERA40 SST with a constant coefficient of -40 $W.m^{-2}.K^{-1}$. In the formulation of the surface salinity distribution, no salinity damping is applied [*Beuvier et al.*, 2010].

The first 7 years of the simulation (1958-1965) were considered as a spi-nup period and were not used in the clustering method. In the following, the 46-year study period extends from 1966 to 2011.

3. The clustering method

As the surface circulation in the SC is highly variable, we try to identify the principal modes of the circulation by analyzing the long-term numerical simulation of *Beuvier et al.* [2012a] allowing some representativity of the inter-annual variations of the Mediterranean general circulation [*Palmieri et al.*, 2015; *Ayache et al.*, 2015]. We apply an efficient clustering method ($SOM + HAC$ here-after) performed in two steps (Figure 2). First, a Self Organising Map algorithm (SOM here-after) is applied to the daily outputs of the simulation and gives different typical situations of the SC surface circulation. Then, a Hierarchical Ascendant Classification algorithm (HAC here-after) is applied to these situations in order to aggregate them into a small number of classes facilitating their interpretation as physical processes. The SOM is well adapted to the problem we solve. It has a higher discriminant power to separate the different classes than the Empirical Orthogonal Functions (EOF) [*Lorenz*, 1956] or the K-Means algorithm [*Badran et al.*, 2005] due the topological constrain among the different classes. Besides the SOM is able to deal with non-linear aspects of the phenomenon that we analyze, contrary to EOF, which mainly deals with linear aspects of the phenomena.

3.1. The *SOM* method

After several trials using different combinations of the daily MED12 outputs, we found that the SC surface circulation can be statistically represented by the two components of the horizontal current vector at 30-m depth taking on a sub-grid of MED12 (Figure 3). This subgrid is not homogeneous because it was specially designed to capture the regions where the different streams are the most significant, in particular to capture the well known streams AC, BTC, ATC and AIS. The 30-m depth represents a good signature of the AW salinity minimum characterizing the Algerian Current. The obtained SC sub-grid contains 176 points (88 dots in Figure 3, for U and V, i.e. $88 \times 2 = 176$) representative of the major key features of the large-scale surface circulation. Each daily surface circulation situation i is thus represented by a vector (U_{SCi},V_{SCi}) of $88 \times 2 = 176$ components. From the 46 years (1966-2011) considered, we obtained a learning data set of 16801 daily situations on the SC sub-grid, typically (U_{SCi},V_{SCi}) in Figure 2, describing the SC surface circulation. This number is an optimum compromise between the information embedded in the database we processed and the ability of the SOM to analyze a high-dimension vector data set. These particular vectors thus correspond to a multivariate data set and are denoted the learning data set of the SOM.

The neural network classifier SOM is an unsupervised classification method consisting of a competitive neural network structured in two layers. The first layer, which is the input layer, receives the multivariate data set D to cluster (the 88×2 velocity components U_{SCi}, V_{SCi} sampled in the channel). The second layer is a 2D-neural grid representing m classes, with a topological ordering and resuming optimally the learning data set D. Each neuron j is associated with a reference vector W_j characterizing a subset of D that gathers data

having common statistical characteristics (usually not linear). The objective of the SOM is hence to summarize the information contained in a multivariate set D by producing a small number m of reference vectors W_j, which are statistically representative of D. The reference vectors W_j on the map aim at approximating the density of the data set D. They are computed through an iterative learning process by minimizing a specific non-linear cost function as in the K-Means algorithm [*Badran et al.*, 2005].

Following our previous study [*Jouini et al.*, 2013], we applied the SOM training process (available on the web site http://www.cis.hut.fi/projects/somtoolbox/download/) in order to summarize the information contained in this data set. We then produced a small number of reference vectors characterizing it. Each reference vector, represents a set of vectors of the simulation that are close to each other, and corresponds to a typical surface circulation regime of the SC.

The number of neurons determines the granularity of the mapping, which in turn is responsible for the accuracy and the SOM map's generalization capabilities. The different neurons of the topological map are connected and thus determine a topological (neighbourhood) relationship between the different neurons. Close neurons on the maps correspond to reference vectors that are quite similar, while very distant neurons correspond to reference vectors that are very different. The topological map (Figure 4a) was learned according to the procedure described in *Niang et al.* [2003] and *Niang et al.* [2006]. The number of neurons was determined empirically from solutions of similar problems and then adjusted, as described in *Badran et al.* [2005]. In the present study, we used a SOM map of $m = 6 \times 7 = 42$ neurons, which corresponds to a quite large number of reference vectors.

3.2. The *HAC* method

With the *SOM* algorithm we have thus clustered the 16801 initial circulation situations into $m = 42$ typical circulation regimes providing a highly discriminating representation of the circulation of the study area, which is difficult to interpret in terms of physical processes. We then applied a *HAC* method (Figure 2) in order to cluster the 42 circulation regimes into a small number of classes, which synthesizes the geophysical information embedded in the data, such as spatial, seasonal or inter-annual specificities. This corresponds to the second step of our *HAC* + *SOM* algorithm.

The *HAC* algorithm is a bottom-up hierarchical classification [*Jain and Dubes*, 1988; *Jain et al.*, 1999]. This method iteratively computes a partition hierarchy [*Badran et al.*, 2005]. From the initial partition containing the neuron groups of the *SOM* map, two neurons of the same neighbourhood are regrouped at each iteration. These two subsets are selected by measuring their similarity according to the Ward criteria. The iterations continue until all the subsets of the partition are regrouped together.

The corresponding circulation regimes of the 42 neurons were aggregated into 8 significant classes (for simplification, only 4 classes are schematized in Figure 2). The resulting clustering of the 176-dimension vectors associated with the neurons of the topological map is given in Figure 4b. Classes 1 and 2 are characterized by two neurons, classes 3 and 4 by four neurons, Class 8 by six neurons, and, classes 5, 6 and 7 by eight neurons.

We note that the *SOM* + *HAC* algorithm is very coherent, since the classes represent clusters whose neurons are contiguous on the topological map (Figure 4a). The number of classes (8) was selected because it presents the most significant discriminative partition with respect to the full dendrogram of the *HAC* according to two statistical indices

used as metrics for evaluating the clustering quality. Indeed, we varied the number of classes between 1 and 12 and computed for each one the Davies-Bouldin index [*Davies and Bouldin*, 1979] and the gap index [*Tibshirani et al.*, 2001]. The first one is an index that takes into account not only the intra-class homogeneity by comparing the distance between each situation vector and its reference vector, but also the heterogeneity between the different classes. The second one compares the within-class dispersion with that expected under an appropriate null dispersion. The number of 8 classes was selected by minimizing the Davies-Bouldin index and maximizing the gap index.

4. The 8 typical situations

4.1. Pattern description

The corresponding SC circulation maps at 30-m depth, as inferred from the *SOM+HAC* method, are presented in Figure 5. The corresponding maps of the salinity distribution at 30-m depth are given in Figure 6. Vertical sections of density and zonal currents in the first 150 m from the surface in the north and south of Sicily are shown in Figure 7. Table 1 shows the current and gyre acronyms.

The oceanic patterns corresponding to the 8 classes are relatively close to each other and in agreement with previous studies. The four main streams, AC, ATC, AIS, and BTC, are well recognized throughout the classes. The SESG is present in all classes with velocities higher than 0.10 m.s^{-1}. The AC velocities are above 0.20 m.s^{-1} and the ATC velocities range from 0.08 and 0.20 m.s^{-1}. Meandering and bifurcations of the ATC are noticed too; the BATC is found in classes 4 to 7 and the ALC is found in classes 1 to 5 and 8. Mesoscale patterns of the AIS are simulated; the ABV (Adventure Bank Vortex) is noticed in classes 2 (barely) and 6, and the MCC (Maltese Channel Crest) is present in

classes 2 to 6. The most striking feature according to this classification is the evidence of a new current, flowing westwards along the northern coast of Sicily, that is flowing in the opposite direction of the BTC (Figure 5). This current is present in classes 3, 4, and 6 to 8, with velocity values varying between 0.03 and 0.08 m.s^{-1} at 30 m depth (Figure 7). It feeds the AIS with Tyrrhenian Sea water composed of AW characterized by a higher salinity by 0.3 than the AW coming from the AC (Figures 6c,d,f,g,h). Another important feature is the like-disappearance of the AIS in Class 1 and Class 7, with very low velocities of 0.04 m.s^{-1} in the 30-m depth AIS core (Figure 7a,m).

In this simulation and according to the classification, the ATC and the SESG are permanent features of the circulation, whereas the AIS may disappear in some classes (Class 1 and Class 7). A new feature appears in five classes (classes 3, 4, 6, 7 and 8): a westward coastal current north of Sicily, denoted the Tyrrhenian Sicilian Current (TSC) here-after, which advects surface Tyrrhenian Sea water characterized by a higher salinity as compared to the AW salinity outflowing from the Algerian Basin into the Ionian Basin. The TSC appears to be an important feature of the circulation as well as the BTC, which is simulated in almost all classes except Class 3.

4.2. Seasonal and inter-annual variabilities

The seasonality of the classes is shown in Figure 8. Classes 3, 4, 7 and 8, characterized by a high TSC signature, mainly occur in summer. Classes 1, 5, and 6, characterized by a high ATC signature, mainly occur in winter. Seasonal variations are not a reliable indicator for explaining the very low AIS velocity (the quasi-absence of the AIS) in classes 1 and 7. The relatively high winter signature of the ATC in classes 1, 2, 5 and 7 is qualitatively in agreement with previous studies in winter. The relatively high-velocity

ATC in Class 4, which never occurs in winter, is more surprising, but is in agreement with several hydrographical observations showing a low-salinity signature along the Tunisian side during the whole year [*Sammari et al.*, 1999; *Ben Ismail et al.*, 2012]. Classes 7 and 8 occur from spring to the end of summer with a well developed TSC. Class 7 is characterized by a high-velocity ATC whereas Class 8 is characterized by a high-velocity AIS.

Inter-annual variations are investigated by analyzing the temporal occurrence of the classes during the 46 years of the experiment (Figure 9a). Each month of the 46-year period under study is affected to a class which corresponds to the daily class which is the most frequently encountered during that month. The confidence of that class for a given month is expressed as a percentage which is the number of occurrence days of the class with respect to the number of days in the month. Most of the class confidences are larger than 66%, showing the efficiency of the classification. Classes 7 and 8 are more or less exclusive of each other (Table 4). The alternation of these two classes shows a strong inter-annual variability with a pseudo-period of about a decade. Class 8 is present (in particular in summer) from 1973 to 1984, from 1990 to 1997, and from 2007 to 2010. Class 7 occurs (in particular in summer) from 1967 to 1972, from 1985 to 1988, from 1998 to 2000, from 2002 to 2006, and in 2011. Class 5 predominates from November to January with some alternation with Class 1, while Class 6 predominates during March-April. On the contrary, Class 1 and Class 7 generally occur in the same years. Class 6 is less common or even absent when Class 7 is present. Classes 1 and 2 do not occur every year. Classes 3 and 4 look like classes of transition from a dynamical summer state represented by classes 7 or 8 to a winter state represented by Class 5. That alternation of the classes 7

and 8 with a decadal period cannot directly be related to the BiOS phenomenon, since this phenomenon is poorly reproduced by the numerical model. In fact the simulated circulations in the northern Ionian Basin (not shown), are cyclonic in both classes (with deeper sea surface height in Class 7) and do not correspond to the BiOS.

The high-velocity ATC signature of Class 1 is in agreement with observations in November 1985 reported by *Manzella et al.* [1990]. The ABV, MCC and the high-velocity AIS and low-velocity ATC of Class 8 are in good agreement with the southern Sicily upwelling summer situation documented in the literature [*Zavatarelli and Mellor*, 1995; *Robinson et al.*, 1999] and observed in 1996 by *Lermusiaux and Robinson* [2001]. The Class-8 features in July 2008 are also in agreement with the high-velocity AIS signature, and the ALC signature owing to the ATC moving over the Tunisian continental slope reported by *Placenti et al.* [2013]. During the period 1998 to 2011, the MCC is not present in 1998, 1999 and 2003 (i.e. in Class 7), which confirms the fact that the MCC is not a permanent structure of the circulation, as shown by *Bonnano et al.* [2014]. The present simulation is also in agreement with the results of previous numerical studies. For example, Class 5 corresponds well to the mean circulation of the month of December of the years 2008-2010 reported by *Sorgente et al.* [2011] and to the mean circulation of January 2001 reported by *Béranger et al.* [2004].

4.3. Transport variabilities

The mean eastward surface transports through the SC associated with each class are shown in Figure 10a. The values correspond to the total transport of surface water crossing eastwards the SC (section SS in Figure 3). The median values (red line in Figure 10a), as well as the mean values (red square in Figure 10a), range from about 0.7 to 1.3 Sv (1

sverdrup (Sv) = 10^6 $m^3.s^{-1}$) (Table 3), while minimum and maximum values range from 0.1 to 3.0 Sv. It highlights the fact that the stronger surface inflows into the Eastern Mediterranean occur in classes 1, 2 and 5, associated with high-velocity ATC, ALC, and BATC, and mainly corresponding to autumn-winter seasons, whereas the weaker surface inflows occur in classes 3, 4 and 8 associated with a low-velocity ATC and a high-velocity AIS, and for the most part corresponding to summer-fall seasons.

The net transport through the SC according to each class is very small (Figure 10b, Table 3). The distribution of minimum and maximum of the net transport (Figure 10b) for each class is different from that of the net surface inflow (Figure 10a). There are negative (towards the west for classes 5, 6 and 8) and positive (towards the east for other classes) net transports, but the variance of the net transport (Figure 10b) looks like the variance of the surface transport (Figure 10a). For example, the amplitudes of the variance are very large for Class 1 and Class 5 for both the surface and the net transports, whereas it is two times lower for Class 3 and Class 4 for both the surface and the net transports. The maximum net transports correspond mainly to Class 2 (0.050 Sv) while the minimum transports correspond to Class 6 (-0.090 Sv). Positive values are then for Class 4 (0.040 Sv) and for classes 1, 3 and 7 (<0.035 Sv). Negative values are then for Class 8 (-0.020 Sv) and Class 5 (-0.040 Sv).

In the inter-annual time-series of the monthly net transport (Figure 9b), there were several major changes between 1966 and 2011 in the net transport regimes, with alternatively positive (eastwards, in the range 0 to 0.032 Sv) and negative (westwards, in the range -0.043 to 0 Sv) values. Four periods show a positive net transport: from October 1967 to October 1972, from March 1986 to April 1988, from August 1998 to March 2007, and from

July 2010 to December 2011. A relationship between these alternations of net transport regimes (Figure 9b) and the alternation of Class 7 with classes 6 or 8 in summer-spring (Figure 9a) is highlighted in Table 4. As an example, for the period from 1992 to 1997, the circulation is largely interpreted as situations of classes 5, 6 and 8 (Figure 9a), which all correspond to negative net transports (Table 3). This period is mainly characterized by situations for which Class 8 is present in summer, Class 5 in autumn and winter, and Class 6 in spring (Figure 9a). And for the following period, from 1998 to 2006, for which the net transport is positive (Figure 9b), the circulation is dominated by the situations of classes 1, 3, 4 and 7 (Figure 9a), which all correspond to positive net transports (Table 3). This period is mainly characterized by situations for which Class 7 is present a large part of the year (between February and October).

5. Evidence of a new current: the Tyrrhenian Sicilian Current (TSC)

5.1. Description of the TSC

All the classes show the presence of well identified currents flowing in the SC which have already been described in the scientific literature; i.e. the AC, the ATC and the AIS (Figure 1). These currents are of an irregular distribution according to the class. The definite presence in classes 7 and 8, and 3 and 4, and slightly less definite in Class 6, of a westward coastal current flowing along the northern coast of Sicily (TSC) before entering the Eastern Mediterranean has never been mentioned as a well defined feature of the circulation. *Napolitano et al.* [2003], using numerical experiments run during a summer situation (their Figure 7B), first mentioned it and reported it as a possible effect of open boundary conditions introduced into their high-resolution model. Moreover, the TSC is depicted in Figure 5 of *Béranger et al.* [2004]; it was obtained with a basin-scale

model of similar resolution to that of *Napolitano et al.* [2003]. It is also shown in Figure 8 of *Sorgente et al.* [2011], who used a very-high-resolution ocean model (1/32°). These authors described an anti-cyclonic circulation in summer which they called the WNSC, but this current did not feed the AIS in their simulation; it turned anti-cyclonically into the northern part of the Tyrrhenian Sea.

In order to characterize the TSC, we looked at the SST associated with each class, as well as the corresponding sea-surface height anomaly (Figure 11). A low SST occurring along the southern coast of Sicily is the signature of a coastal upwelling. This upwelling, which is quasi-permanent during the summer months [*Kostianoy et al.*, 1998], often extends up to the eastern and northern coasts of Sicily in our simulation, in particular for classes 3, 4, 7 and 8 (Figures 11c, 11d, 11g, 11h), denoting an upward motion of deep water. This is characterized by a negative sea-surface height anomaly around the Sicily coastline. This kind of signature, characterized by a low-SST water along the southern and western coasts of Sicily, is confirmed by the lower temperature observed from satellite infrared images, in July 2005 and 2010 (Figure 12), and is also found in the low sea-surface height anomaly values in AVISO products (Figure 13e) along the southern and northern coasts of Sicily. Our results are also confirmed by another companion simulation run with a 1/36°-resolution basin-scale model MED36 [*Arsouze et al.*, 2013] forced by the same atmospheric forcing as MED12. The SSTs of MED12 (Figure 13a) and MED36 (Figure 13b) in July 2005 (Class 7) compare very well, as do their temperatures at 30-m depth (Figure 13b, d). In MED36, there is a TSC (somewhat narrower than in MED12) feeding the AIS when the upwelling is well developed. The good agreement of the modelled surface results

(Figure 13a, b) with the satellite observations (Figures 12a and 13e) confirms the realism of the models and consequently of the TSC at 30-m depth (Figure 13c, d).

The TSC therefore appears as a new fact in the SC circulation scheme and it must be taken into account in the interpretation of the characteristics of the surface water flowing eastwards through the SC.

5.2. Origin of the TSC

In our model, the TSC, which flows westwards along the northern coast of Sicily, occurs at the same time as the Sicilian upwelling develops along the southern coast of Sicily, mainly during the summer period. This upwelling is described in the scientific literature as a wind-induced upwelling, since the winds are mostly blowing from the northwest following the loop of the Mistral [*Zavatarelli and Mellor*, 1995]. In order to verify if the wind is a good candidate for driving the upwelling, we computed the correlation coefficient between the time-series of the component of the wind stress parallel to the southern coast of Sicily and the SST off the coast for several time periods of Class 8 for which the upwelling is well defined (Figure 11h). As an example, Figure 13f shows that the wind stress during the 5-day period (9 to 13 July 2005) preceding the upwelling was very low and unable to generate an upwelling. Moreover, the low value of the correlation coefficient (< 0.1) shows that there is no direct link between the northwesterly winds and the SST and consequently with the upwelling.

This implies that other mechanisms must be sought. We therefore investigated the possibility that the upwelling is density-driven. Previous works [*Herbaut et al.*, 1998; *Onken and Sellschopp*, 1998; *Pierini and Rubino*, 2001; *Molcard et al.*, 2002; *Béranger et al.*, 2004] showed the importance of coastal topographic waves for explaining the circulation

in the SC. In particular, *Herbaut et al.* [1998] showed that a boundary coastal jet flowing from left to right along a straight coast (AC in Figure 14a) can split into two branches when encountering a topographic shallow channel situated in the middle of the coast. One branch enters the channel and flows along its left coast as a boundary coastal jet (ATC in Figure 14a); the other crosses the channel, guided by a double Kelvin wave trapped by the channel topography, and then continues to flow along the coastline (BTC in Figure 14a). In these process studies and the associated numerical experiments, the boundary coastal jet representing the AC was generated by a density gradient in the left part of channel coast (Figure 14b).

Molcard et al. [2002] employing a similar reasoning but dealing with a realistic coastline and topography and conducting several numerical sensitivity experiments were able to show that an AIS can be generated by a density gradient between the Western Mediterranean and the Ionian Basin. The velocities of the ATC and of the AIS vary according to the density gradient through the channel [*Pierini and Rubino*, 2001]. These two process studies provide a rational framework for explaining the ATC, the AIS and the BTC. *Béranger et al.* [2004], comparing idealized and realistic configurations, showed that the meandering of the AIS appeared to be associated with the continental slope of the Adventure Bank, as the realistic simulation of *Pierini and Rubino* [2001] has shown. According to a high-resolution modelling using data assimilation techniques, *Onken et al.* [2003] argued that the AIS is triggered by both topography and LIW outflow.

Therefore, it appears that a good candidate for driving the Sicilian upwelling is the presence of a density gradient between the Tyrrhenian Sea and the Ionian Basin, which induces a baroclinic coastal boundary jet [*Molcard et al.*, 2002] in the form of a baroclinic

Kelvin wave, which propagates from the Ionian Basin towards the Tyrrhenian Sea, according to the scheme in Figure 14c. Schematically this baroclinic Kelvin wave of very long wave-length is associated with a deep current, which transports dense Ionian water into the Tyrrhenian Sea and a surface current in the opposite direction transporting Tyrrhenian Sea surface water into the Ionian Basin. This motion can be interpreted in terms of conservation of mass and relative potential vorticity in a two-layer system [*Hsieh and Gill*, 1984]. The dense Ionian water flows at depth along the coast towards the Tyrrhenian Sea. This water is trapped by the coast around the western tip of Sicily and propagates along the northern coast of Sicily. During its progression, this deep Ionian water uplifts the two-layer fluid interface, generating an upwelling along the coast of Sicily (Figure 14d) with a positive vorticity in the lower layer and a negative one in the upper layer, the sum of these two vorticities being constant. In order to satisfy the continuity equation, the low-density Tyrrhenian Sea water (compared to the denser Ionian water) flows in the opposite direction and enters the Ionian Basin forming the TSC in the Tyrrhenian Sea and the AIS in the eastern part of the SC.

5.3. Mechanisms driving the TSC

The simulated results (Figure 5 and Figure 7) are qualitatively in agreement with the density driven forcing described in Section 5.2. In the numerical model, the Kelvin waves found in the idealized scheme of Figure 14d are represented by coastal trapped waves modified by the topography. Figure 15a presents the variability of the density difference between the Ionian Basin and the Tyrrhenian Sea, obtained by averaging the monthly density in the two boxes drawn in Figure 3 in the sub-surface layer between 50 and 150 m

depth. Figure 15b redraws these monthly values in the line of Figure 9 while the 46-year seasonal cycle of this difference is reported in Figure 15c.

As an example in Class 3, which mainly occurs in summer-autumn (Figure 8), the density gradient between the Ionian Basin and the Tyrrhenian Sea is large and the vertical stratification in the Sicily Channel is characterized by strong isopycnal slopes (Figure 7e). These slopes are the signature of the advection of the dense Ionian water into the Western Mediterranean associated with coastal trapped waves propagating towards the Tyrrhenian Sea. The Ionian water isopycns are uplifted to the surface at the coast. Consequently, the sea surface temperature is cooled along the southern Sicily coast as seen in Figure 11c showing a density-driven coastal upwelling. These coastal trapped waves when arriving in the Tyrrhenian Sea generate the TSC as explained in Section 5.2 and evidenced by the negative sea surface height in Figure 11c. Classes 4, 6, 7 and 8 present a similar behavior as this of Class 3 (Figures 7g,k,m,o).

Class 5 mainly occurs in autumn-winter (Figure 8) when the density gradient between the Ionian Basin and the Tyrrhenian Sea is small (Figure 15). It is characterized by flatter isopycnal slopes in the Sicily Channel (Figure 7i). The coastal trapped waves are less energetics and consequently the associated transport of Ionian water into the Western Mediterranean is weaker. These waves are not enough energetics to force the TSC when arriving in the Tyrrhenian Sea. Classes 1 and 2 present a similar behavior as this of Class 5.

These behaviors fit the theoretical schemes shown in Figure 14. Besides, in all the classes, one can observe a slow westward current of dense Ionian water close to the Sicilian shelf, whose maximum velocities 0.012 $m.s^{-1}$ is encountered at 110 m depth above the

Adventure Bank. It is up to 50 m depth in Class 5 and reaches 10 m depth in Class 3 with a maximum of 0.010 m.s^{-1}.

The forcing mechanism of this westward current along the southern Sicily is enhanced by the Ionian water spreading through the SC towards the Tyrrhenian Sea. Figure 15a confirms that the density gradient which exists between the Ionian Basin and the Tyrrhenian Sea at intermediate depths, is at the origin of the westward sub-surface current of Ionian water (schematized by ρ_3 in Figure 14d). Classes 3, 4, 7, 8 occurred mainly in spring-summer and Class 6 in spring-summer, when the density gradient is larger than in autumn-winter for which classes 1, 2, 5 occurred. A correlation is suspected between the inter-annual variability of this density gradient (Figure 15b) and the alternation of Class 7 and Class 8 (Figure 9a), high gradient values corresponding to Class 7 and low values to Class 8, in agreement with the results presented in Figure 9b, in which Class 7 (high gradients values) corresponds to a net westward transport and Class 8 (low gradient values) to a net eastward transport.

6. Summary and Conclusions

We analyzed the surface circulation in the Sicily Channel provided by a 46-year run of the high-resolution model MED12. The aim was to evidence the most characteristic modes of the circulation. For that, we used a high-performance clustering method, the SOM, which is a non-parametric neural method widely used in many research fields. We decomposed the circulation into 8 major classes, whose the shortest duration can last several weeks, and the longest, several months. Current and salinity maps according to each class confirmed the AW spreading into three main well known branches, the ATC, the BTC and the AIS. A new branch of the SC circulation has been also highlighted by

these maps, the so-called TSC which streams along the northern coast of Sicily and brings Tyrrhenian Sea surface water into the Eastern Mediterranean. The 8 modes present a well-marked seasonality. Some of them occur mainly in summer (Classes 3, 4, 7 and 8) or in spring (Classes 6 and 7), some others in winter (Classes 1 and 5) and in autumn (Classes 2 and 3). The major features characterizing the modes are the relative importance of the ATC versus the AIS, or the presence of the TSC versus the BTC, in most of the classes, the all-year-round presence of the SESG. In particular, several classes show the quasi absence of the AIS (Classes 1 and 7). Some classes (Classes 1 and 2) appeared only at an inter-annual scale. The classes are associated with well marked hydrographical features. Most of the summer classes 8, 7, 4, 3 are associated with a strong upwelling along the southern coast of Sicily. The net transport through the Sicily Channel varies at an inter-annual scale of about 10 years. A class alternation is associated with this net transport variation, Classes 1 to 4 and 7 corresponding to positive net transport, and classes 5, 6 and 8 corresponding to negative net transport.

Correlation between the component of the wind parallel to the coast and the SST off the southern coast of Sicily is very weak, showing that the wind does not play a role in forcing this upwelling. This interpretation is re-enforced by the fact that the upwelling bypasses the western tip of Sicily, reaching the northern coast of Sicily, as seen in negative sea-surface height anomaly contours around Sicily and the presence of low SST on the northern coast of Sicily. This is in agreement with a density-driven upwelling associated with the propagation of Ionian Basin water trapped along the coast as a coastal baroclinic topographic wave responsible for the advection of Ionian Basin water into the Tyrrhenian Sea. Besides the Mistral-like wind, which quite often blows in the SC region in summer,

has a large spatial structure with respect to the western tip of Sicily. It generates an Ekman transport, which favours upwelling along the southern coast and downwelling along the northern coast of Sicily, showing that such a wind cannot generate an upwelling on both sides of the coast, as can be seen in the satellite observations and in Class 8 for the model results. The TSC and the upwelling are consequently the signature of the density forcing of the circulation in the SC.

All these facts lead us to conclude that the surface circulation and the hydrographical structures of the SC are mainly density-driven. We have evidence of the importance of the TSC, which is present in most of the classes. The TSC and the AIS are strongly linked, since they are driven by the entry of the dense Ionian Basin water at intermediate depth (50-150 m) into the Tyrrhenian Sea, which uplifts the interface separating the surface water and the deeper water, generating the southern Sicily coastal upwelling and also the upwelling occurring at the eastern tip of Sicily and along the northern coast of Sicily. This new description of the surface circulation, which was evidenced in the analysis of the outputs of MED12 and MED36, is also present in other models, such as that of *Sorgente et al.* [2011] and in good agreement with satellite SST observations for different years. Moreover, the model results can be interpreted through a theoretical framework involving coastal topographic baroclinic waves, in the light of the works of *Herbaut et al.* [1998] and *Molcard et al.* [2002]. The forcing of these motions is the density gradient which exists between the Ionian Basin and the Tyrrhenian Sea The seasonal variations of this density gradient are correlated with the occurrences of classes presented in Figure 9. Classes 3, 4, 6, 7, and 8 occur in spring-summer when the density gradient is large while classes occur 1, 2, 5 in winter when the density gradient is minimum. Moreover a qualitative

correlation is observed between the inter-annual variability of this density gradient and the alternation of Class 7 and Class 8, high gradient values corresponding to Class 7 (Figure 15a) and low values to Class 8, in agreement with the results presented in Figure 9, in which Class 7 (high gradients values) corresponds to a net westwards transport and Class 8 (low gradient values) to a net eastward transport.

By analyzing 46 years of MED12 outputs, we were able to propose a new description of the circulation in the Sicily Channel, which is synthetized in Figure 1. We strongly recommend new observations with drifters or current-meter moorings at the northern entrance of the SC and along the northern coast of Sicily to provide more evidence for the reality of the TSC signature.

Acknowledgments.

This work was supported by the following French and European agencies: Mercator Ocean (www.mercator-ocean.fr) and the DGA for the SiMED project, and the GIS for the MORCE project. Atmospheric forcing data sets were made available by CNRM. This work was granted access to the HPC resources of IDRIS of the CNRS under project 010227 made by GENCI. The financial support of J. Beuvier's Ph.D was provided by Météo-France. We thank Michel Déqué of Météo-France for running the ARPERA simulation with ARPEGE-Climat. The realization of the GLORYS1 global ocean reanalysis had the benefit of the grants that the GMMC, and INSU-CNRS and the support of the European Union via the MyOcean project. We thank Bruno Levier of Mercator Ocean for gathering the bathymetry products. We acknowledge the GEBCO-08 Grid, version 20081212, http ://www.gebco.net, for providing the GEBCO-08 bathymetry. The altime-

ter products were produced by Ssalto/Duacs and distributed by AVISO, with support from CNES (http ://www.aviso.oceanobs.com/duacs/). We also aknowledge the GOS team, http ://gos.ifa.rm.cnr.it/index.php, and the MyOcean project for providing the GOS-SST product. NOAA/AVHRR images are acquired at CMS and are provided in brightness temperatures by SATMOS. This work is a contribution to the HyMeX international programme on the study of the water cycle in the Mediterranean area and the MED-CORDEX programme.

Figure Captions

Figure 1. Scheme of the Atlantic Water circulation in the Sicily Channel (SC) area mainly summerized by *Sorgente et al.* [2011], with permanent patterns in *black* lines, summer patterns in *red* lines, and winter patterns in *blue* lines. Note that the Maltese Channel Crest (MCC) is drawn as an anti-cyclone (as in *Béranger et al.* [2004] and in *Lermusiaux and Robinson* [2001]). The new feature highlighted by this study, the Tyrrhenian Sicilian Current (TSC), is added in *red* because it is preferably simulated in summer. Corresponding acronyms are in Table 1. The bathymetry is drawn using a grey scale to highlight the shallow continental shelves in the Central Mediterranean (m). L is Lampedusa Island.

Figure 2. Schematic representation of the two steps of the clustering method $SOM + HAC$. (1) Structure of the self-organizing map (SOM): The network comprises two layers: an input layer used to present observations (88 current component daily values U_{SC} and V_{SC} at 30 m depth provided by the MED12 simulation covering the period 1966-2011) and an adaptation layer with 42 neurons (represented in colour). Each neuron is associated with a reference vector representing a set of U and V having close similarities representing a typical channel circulation. A neuron neighbourhood system is defined (schematized by the *blue* arrows) on the adaptation layer. (2) The 42 groups are clustered in 8 classes by the HAC algorithm, which is schematized by vertical sticks. For simplicity, only 4 classes are shown in the figure (*blue*, *red*, *green* and *yellow* neurons).

Figure 3. Definition of the SC sub-grid for application of the *SOM* method. The bathymetry of the MED12 model is drawn according to the *grey scale* given on the right-hand side of the figure. The *white* dots represent the 88 coordinates of the SC sub-grid composed of the (176 values = 2×88) U and V components of the 30-m depth currents. This corresponds to a sub-grid increment of $\Delta x \approx 15$ km along the x-axis in the W-E direction and to a sub-grid increment of $\Delta y \approx 25$ km along the y-axis in the N-S direction. The *black* line represents the area [33.5-39.5°N;7-15°E] covered by the maps of classes in Figures 5, 6 and 11. The *black* line between Tunisia and Sicily (SS) represents the SC section used for transport calculation reported in Table 3, and in Figures 9b and 10. The *red* lines (TYR) north and (SSI) south of Sicily represent the vertical sections in Figure 7. The 2 *blue* boxes, T-box in the Tyrrhenian Sea and I-box in the Ionian Basin, are used for calculation in Figure 15.

Figure 4. *(a: upper panel)* The topological map shows the distances between neurons (ranged from 5 to 10.5 according to the colour bar) and the corresponding classes. Each neuron is associated with a class. The classes are numbered from 1 to 8. *(b: bottom panel)* Neural map of the 8 classes obtained from the $SOM + HAC$ algorithm. The 8 classes are represented by different colours. The number of neurons is two for classes 1 and 2, four for classes 3 and 4, six for Class 8, and eight for classes 5, 6 and 7.

Figure 5. Maps of currents (modulus and vectors in $\mathrm{m.s}^{-1}$) at 30-m depth for the 8 classes for the zoomed area indicated in Figure 3. Only one vector in every two is plotted.

Figure 6. Maps of salinity at 30-m depth for the 8 classes for the zoomed area indicated in Figure 3 (contours every 0.1).

Figure 7. Vertical sections of density and currents along (left panels) south of Sicily (*red* line SSI in Figure 3) and (right panels) north of Sicily (*red* line TYR in Figure 3), for the classes 1 to 4. The eastward velocities (positive values) are drawn in *full black* lines while the westward velocities are drawn in *dashed black* lines. *Black* contours are every 0.01 $m.s^{-1}$ whereas the *white* line shows the zero velocity. In the left panels, the *dashed blue* contours represent the westward velocities between -0.001 and -0.009 $m.s^{-1}$ every 0.001 $m.s^{-1}$.

Figure 7 (continued). for the classes 5 to 8.

Figure 8. The x-axis represents the numbered classes, while the y-axis indicates the percent of seasonal occurrence of each class drawn in colors (DJF in *blue*, MAM in *green*, JJA in *red*, SON in *brown*) (for example, the sum of the DJF values is 100%).

Figure 9. *(a: upper panel)* Time variability of the 8 classes: The x-axis represents the years from 1966 to 2011, while the y-axis indicates the months. The classes are identified by a color scale on the right of the figure. A month is affected to the class whose the daily class is the most frequently encountered during that month. The monthly confidence of that class is expressed as a percentage which is the number of occurrence days of the class with respect to the number of days in the month. Plain colors correspond to

months whose class confidences are larger than 66%, striped color to months whose class confidences are between 66% and 33%. Most of the class confidences are larger than 66%, showing the efficiency of the classification. *(b: bottom panel)* Time-series of the monthly net transport through the SC, in sverdrups (Sv), from 1966 to 2011, filtered with a 3-year time-window (positive is eastwards).

Figure 10. Box-and-whisker plots of the eastward *(a: upper panel)* and the net *(b: bottom panel)* transports (in sverdrups, Sv) through the SC for each class. The *blue* box extends from the lower to the upper quartile values, with a *red* line at the median and a *red* square at the mean. The end of the whiskers is 1.5 times the inter-quartile range past the first and third quartiles. Outliers are plotted as individual points.

Figure 11. Sea-surface temperature (°C) for the 8 classes of Figure 5 and the associated sea-surface height anomaly represented at a contour interval of 0.02 $m.s^{-1}$.

Figure 12. NOAA/AVHRR thermal images in 13 July 2005 *(a: left panel)* and in 22 July 2010 *(b: right panel).*

Figure 13. Snapshots of sea-surface temperature (°C) and currents ($m.s^{-1}$) *(top panel)* and 30-m depth potential temperature and currents *(middle panel)* for MED12 (a, c) and MED36 (b, d) simulations forced by (f) the same wind stress ($N.m^{-2}$) from ARPERA *(bottom panel, f).* AVHRR sea-surface temperature from GOS [*Breivik et al.*, 2014] overplotted by the geostrophic currents and zero sea-surface height anomaly contour from

AVISO [*CLS*, 2008] (bottom panel, e). Note that the colourbar of the model sea-surface temperature is shifted by -0.5°C and the sea-surface height anomaly of the model is shifted by 0.085 m. All the ocean fields are from 15 July 2005, whereas the wind stress is from 11 July 2005. That wind, which is characterized by stress values lower than 0.05 $N.m^{-2}$, corresponds to the strongest winds occuring in the model during the 4-day period from 11 to 14 July 2005. Only one vector in every two is plotted in MED12 and ARPERA, and only one in every four in MED36.

Figure 14. Schematic functioning of the surface currents in the Sicily Channel. The *thin black* arrows show the propagation of the Kelvin wave fronts. The double arrows show the double Kelvin wave. (a) and (c) represent horizontal sections of the Sicily Channel, the horizontal *black* segments represent the position of the vertical section (b) and (d) crossing the channel. The two *upper panels* show a schematic formation of the ATC and BTC from the AC, according to *Herbaut et al.* [1998], (a) represents the surface currents (*thick grey* arrows) in the channel region. The vertical double line represents the water reservoir of AW (density $\rho_1 < \rho_2$) whose opening generates the Kelvin coastal jet. (b) represents a vertical section of the inflow of low-density water (in *white*) advected by the ATC into the channel over denser Eastern Mediterranean water (in *grey*). The two *lower panels* show a schematic explanation of the AIS and TSC formation following the mechanism suggested by *Molcard et al.* [2002]. (c) represents the surface currents (*thick grey* arrows) in the channel region. These currents are forced by the density gradient between the Tyrrhenian Sea and the Ionian Basin. Note that the surface currents flow in the opposite direction to that of the Kelvin wave front. The vertical double line represents the water reservoir

of dense Eastern Mediterranean water (density $\rho_3 > \rho_2$) whose opening generates the Kelvin coastal jet. (d) shows the inflow of Eastern Mediterranean water (in *grey*) into the Tyrrhenian Sea which contributes to uplifting the water interface along the southern coast of Sicily, favouring the upwelling.

Figure 15. (a-top) Time-series of the density gradient between the Ionian Basin and the Tyrrhenian Sea according to the monthly density differences calculated by averaging the Ionian and Tyrrhenian densities in two boxes (I-box and T-box, respectively, Figure 3) in the subsurface layer (50-150m). (b-middle) The *x-axis* represents the years from 1966 to 2011, while the *y-axis* indicates the months. The density differences of (a) ranged between 0.2 and 0.8 kg.m^{-3} according to the given color scale on the right-hand side of the figure. (c-bottom) Climatological seasonal cycle of (a).

Table Captions

Table 1. Acronyms of Mediterranean oceanic features in the Sicily Channel.

Table 2. Acronyms used in the text.

Table 3. Values of the mean and median eastward and net transports (in sverdrups, Sv) through the SC for each class (see Figure 9).

Table 4. Number of months for each period for which classes 7 and 8 are present and the corresponding sign of the net eastward transport according to Figure 8.

References

Arsouze, T., J. Beuvier, K. Béranger, S. Somot, C. Lebeaupin Brossier, R. Bourdallé-Badie, and Y. Drillet (2013), Sensibility analysis of the Western Mediterranean Transition inferred by four companion simulations, *CIESM Congress, Marseille*.

Astraldi, M., G. Gasparini, A. Vetrano, and S. Vignudelli (2002), Hydrographic characteristics and interannual variability of water masses in the central Mediterranean: a sensitivity test for long-term changes in the Mediterranean Sea, *Deep-Sea Research I*, *49*, 661–680.

Ayache, M., J.-C. Dutay, P. Jean-Baptiste, K. Béranger, T. Arsouze, J. Beuvier, J. Palmieri, B. Le Vu, and W. Roether (2015), Modelling of the anthropogenic tritium transient and its decay product helium-3 in the Mediterranean Sea using a high-resolution regional model, *Ocean Science*, *11*, 323–342, doi:10.519/os-11-323-2015.

Badran, F., M. Yacoub, and S. Thiria (2005), chap. Self-Organizing Maps and Unsupervised Classification, pp. 379–442, Neural Networks, Springer Berlin Heidelberg, doi: 10.1007/3-540-28847-3.

Barnier, B., G. Madec, T. Penduff, J.-M. Molines, A.-M. Treguier, J. Le Sommer, A. Beckmann, A. Biastoch, C. Boning, J. Dengg, C. Derval, E. Durand, S. Gulev, E. Remy, C. Talandier, S. Theetten, M. Maltrud, J. McClean, and B. De Cuevas (2006), Impact of partial steps and momentum advection schemes in a global ocean circulation model at eddy-permitting resolution, *Ocean Dynamics*, *56*, 543–567.

Ben Ismail, S., C. Sammari, G.-P. Gasparini, K. Béranger, M. Brahim, and L. Aleya (2012), Water masses exchanged through the Sicily Channel: evidence for the presence of new water masses on the Tunisian side of the Channel, *Deep-Sea Research I*, *63*,

65–81, doi:10.1016/j.dsr.2011.12.009.

Béranger, K., L. Mortier, G.-P. Gasparini, L. Gervasio, M. Astraldi, and M. Crépon (2004), The dynamics of the Sicily Strait: A comprehensive study from observations and models, *Deep Sea Research II*, *51*, 411–440.

Béranger, K., L. Mortier, and M. Crépon (2005), Seasonal variability of water transports through the Straits of Gibraltar, Sicily and Corsica, derived from a high resolution model of the Mediterranean circulation, *Progress in Oceanography*, *66(2-4)*, 341–364.

Béthoux, J.-P., and B. Gentili (1999), Functioning of the Mediterranean Sea: past and present changes related to freshwater input and climate changes, *Journal of Marine Systems*, *20*, 33–47.

Béthoux, J.-P., and D. Tailliez (1994), chap. Deep-water in the western Mediterranean Sea, yearly climatic signature and enigmatic spreading, pp. 355–369, In: Malanotte-Rizzoli, P., Robinson, A.R. (Eds.), Ocean Processes in Climate Dynamics: Global and Mediterranean Examples. Kluwer Academic Publishing, Dordrecht.

Beuvier, J., S. F., M. Herrmann, H. Kontoyiannis, W. Ludwig, M. Rixen, E. Stanev, K. Béranger, and S. Somot (2010), Modelling the Mediterranean Sea interannual variability over the last 40 years: focus on the EMT, *Journal of Geophysical Research*, *115*, C08017, doi:10.1029/2009JC005,950.

Beuvier, J., C. Lebeaupin Brossier, K. Béranger, T. Arsouze, R. Bourdallé-Badie, C. Deltel, Y. Drillet, P. Drobinski, N. Ferry, F. Lyard, F. Sevault, and S. Somot (2012a), MED12, oceanic component for the modeling of the regional Mediterranean earth system, *Mercator Ocean Quaterly Newsletter 46, Special Issue NEMO-MyOcean*, *November*, 60–66.

Beuvier, J., K. Béranger, C. Lebeaupin Brossier, S. Somot, F. Sevault, Y. Drillet, R. Bourdallé-Badie, N. Ferry, and F. Lyard (2012b), Spreading of the Western Mediterranean Deep Water after winter 2005: Time scales and deep cyclone transport, *Journal of Geophysical Research*, *117*, C07022, doi:10.1029/2011JC007,679.

Blanke, B., and P. Delecluse (1993), Variability of the Tropical Atlantic Ocean Simulated by a General Circulation Model with Two Different Mixed-Layer Physics, *Journal of Physical Oceanography*, *23*, 1363–1388.

Bonnano, A., F. Placenti, G. Basilone, R. Mifsud, S. Genovese, B. Patti, M. Di Bitetto, S. Aronica, M. Barra, G. Giacalone, R. Ferreri, I. Fontana, G. Buscaino, G. Tranchida, E. Quinci, and S. Mazzola (2014), Variability of water mass properties in the Strait of Sicily in summer period of 1998-2013, *Ocean Science*, *11*, 811–837, doi:10.5194/osd-11-811-2014.

Breivik, L.-A., B. Buongiomo Nardelli, C. Tronconi, and A. Pisano (2014), *Product User Manual for reprocessed leval 4 SST products over the Mediterranean and Black Seas*, MyOcean, Project FP7-SPACE-20011-1.

Ciappa, A. (2009), Surface circulation pattern in the Sicily Channel and Ionian Sea as revealed by MODIS chlorophyll images from 2003 to 2007, *Continental Shelf Research*, *29(17)*, 2099–2109.

CLS (2008), *Argos users manual*, CLS, http: //www.aviso.oceanobs.com, http://www.argossystem.org/.

Daget, N., A. T. Weaver, and M. A. Balmaseda (2009), Ensemble estimation of background-error variances in a three-dimensional variational data assimilation system for the global ocean, *Quaterly Journal of the Royal Meteorological Society*, *135*,

1071–1094.

Davies, D., and D. Bouldin (1979), A cluster separation measure. Pattern Analysis and Machine Intelligence, *IEEE Transactions on*, *2*, 224–227.

Fernandez, V., D. E. Dietrich, R. L. Haney, and J. Tintore (2005), Mesoscale, seasonal and interannual variability in the Mediterranean Sea using a numerical ocean model, *Progress in Oceanography*, *66(2-4)*, 321–340.

Ferry, N., L. Parent, G. Garric, B. Barnier, N. Jourdain, and the Mercator-Ocean-team (2010), Mercator Global Eddy Permitting Ocean Reanalysis GLORYS1V1: Description and Results, *Mercator Ocean Quarterly Newsletter*, *36*, 15–28.

Gacic, M., G. L. Eusebi Borzelli, G. Civitarese, V. Cardin, and S. Yari (2010), Can internal processes sustain reversals of the ocean upper circulation? The Ionian Sea example, *Geophysical Research Letters*, *37(L09608)*.

Gerin, R., P.-M. Poulain, I. Taupier-Letage, C. Millot, S. Ben Ismail, and C. Sammari (2009), Surface circulation in the Eastern Mediterranean using Lagrangian drifters (2005-2007), *Ocean Science*, *5*, 559–574.

Hamad, N., C. Millot, and I. Taupier-Letage (2006), The surface circulation in the eastern basin of the Mediterranean Sea, *Scientia Marina*, *70(3)*, 457–503.

Herbaut, C., F. Codron, and M. Crépon (1998), Separation of a coastal current at a strait level : case of the strait of Sicily, *Journal of Physical Oceanography*, *28*, 1346–1362.

Herrmann, M., and S. Somot (2008), Relevance of ERA40 dynamical downscaling for modeling deep convection in the Mediterranean Sea, *Geophysical Research Letters*, *35(L04607)*, doi:10.1029/2007GL032442.

Hsieh, W. H., and A. E. Gill (1984), Rossby adjustment problem in a rotating stratified channel, with and without topography, *Journal of Physical Oceanography*, *14*, 424–437.

Jain, A., and R. Dubes (1988), *Algorithms for clustering Data*, Prentice-Hall, Englwood Cliffs.

Jain, A., M. Murty, and P. Flynn (1999), Data clustering: a review, *ACM Computing Surveys*, *31*, 264–323.

Jouini, M., M. Lévy, M. Crépon, and S. Thiria (2013), Reconstruction of satellite chlorophyll images under heavy cloud coverage using a neural classification method, *Remote Sensing of Environment*, *131*, 232–246, doi:10.1016/j.rse.2012.11.025.

Kohonen, T., and P. Somervuo (2002), How to make large self-organizing maps for nonvectorial data, *Neural Networks*, *15*, 945–952, doi:10.1016/S0893-6080(02)00069-2.

Kostianoy, A., M. Astraldi, G. Gasparini, and S. Vignudelli (1998), *Variability of the Sicilian upwelling, Oceanic Fronts and related Phenomena*, Konstantin Federov Memorial Symposium, Pushkin.

Lacombe, H., P. Tchernia, and L. Gamberoni (1985), Variable bottom water in the western Mediterranean, *Progress in Oceanography*, *14*, 319–338.

Lebeaupin Brossier, C., K. Béranger, C. Deltel, and P. Drobinski (2011), The Mediterranean response to different space-time resolution atmospheric forcings using perpetual mode sensitivity simulations, *Ocean Modelling*, *36(1-2)*, 1–25.

Lermusiaux, P. (1999), Estimation and study of mesoscale variability in the Strait of Sicily, *Dynamics of Atmospheres and Oceans*, *29*, 255–303.

Lermusiaux, P., and A. Robinson (2001), Features of dominant mesoscale variability, circulation patterns and dynamics in the Strait of Sicily, *Deep-Sea Research I*, *48*, 1953–

1997.

Levitus, S., J. Antonov, and T. Boyer (2005), Warming of the world ocean, 1955-2003, *Geophysical Research Letters*, *32*, (L02,604).

Liu, Y., R. Weisberg, and L. Shay (2007), Current Patterns on the West Florida Shelf from Joint Self-Organizing Map Analyses of HF Radar and ADCP Data, *Journal of Atmospheric and Oceanic Technology*, *24*, 702–712.

Lorenz, E. N. (1956), Empirical Orthogonal Functions and Statistical Weather Prediction, *Technical Report 1, Statistical Forecasting Project Report, Department of Meteorology, Massachussets Institute of Technology, Cambridge, Massachussetts*, *1*, 1–49.

Ludwig, W., E. Dumont, M. Meybeck, and S. Heussner (2009), River discharges of water and nutrients to the Mediterranean and Black Sea: Major drivers for ecosystem changes during past and future decades ?, *Progress in Oceanography*, *80*, 199–217.

Lyard, F., F. Lefevre, T. Letellier, and O. Francis (2006), Modelling the global ocean tides: modern insights from FES2004, *Ocean Dynamics*, *56(5-6)*, doi:10.1007/s10236-006-0086-x.

Madec, G., and The-NEMO-Team (2008), *NEMO ocean engine*, Technical report,Institut Pierre-Simon Laplace (IPSL), N°27, ISSN: 1288-1619, France.

Manzella, G., T. Hopkins, P. Minnett, and E. Nacini (1990), Atlantic water in the Strait of Sicily, *Journal of Geophysical Research*, *95(C2)*, 1569–1575.

Mihanovic, H., S. Cosoli, I. Vilibic, D. Ivankovic, V. Dadic, and M. Gacic (2011), Surface current patterns in the northern Adriatic extracted from high-frequency radar data using self-organizing map analysis, *Journal of Geophysical Research*, *116(C08033)*, doi: 10.1029/2011JC007104.

Millot, C., and I. Taupier-Letage (2005), *The handbook of environmental chemistry, Vol.1*, chap. Circulation in the Mediterranean Sea, pp. 29–66, Springer-Verlag, doi: 10.1007/b107143.

Molcard, A., L. Gervasio, A. Griffa, G. Gasparini, L. Mortier, and T. Ozgokmen (2002), Numerical investigation of the Sicily Channel dynamics: density currents and water mass advection, *Journal of Marine System*, *36(3-4)*, 219–238.

Napolitano, E., G.-M. Sannino, V. Artale, and S. Marullo (2003), Modeling the baroclinic circulation in the area of the Sicily channel: The role of stratification and energy diagnostics, *Journal of Geophysical Research*, *108(C7), 3230*, doi:10.1029/2002JC001502.

Niang, A., L. Gross, S. Thiria, F. Badran, and C. Moulin (2003), Automatic Neural Classification of Ocean Colour Reflectance Spectra at the Top of the Atmosphere with Introduction of Expert Knowledge, *Remote Sensing of Environment*, *86(2)*, 257–271.

Niang, A., F. Badran, C. Moulin, M. Crépon, and S. Thiria (2006), Decoding aerosol typology and optical thickness over the Mediterranean from SeaWifs images using neural methodology, *Remote Sensing of Environment*, *100*, 82–94.

Olita, A., S. Dobricic, A. Ribotti, L. Fazioli, A. Cucco, C. Dufau, and R. Sorgente (2012), Impact of SLA assimilation in the Sicily Channel Regional Model: model skills and mesoscale features, *Ocean Science*, *8*, 485–496.

Onken, R., and M. Sellschopp (1998), Seasonal variability of flow instabilities in the Strait of Sicily, *Journal of Geophysical Research*, *103(C11)*, 24,799–24,820.

Onken, R., A. Robinson, P. Lermusiaux, P. J. Haley, and L. Anderson (2003), Data-driven simulations of synoptic circulation and transports in the Tunisia-Sardinia-Sicily region, *Journal of Geophysical Research*, *108(C9)*, 8123–8136.

Palmieri, J., J. Orr, J.-C. Dutay, K. Béranger, A. Schneider, J. Beuvier, and S. Somot (2015), Simulated anthropogenic CO_2 storage and acidification of the Mediterranean Sea, *Biogeosciences*, *12*, 781–802, doi:10.5194/bg-12-781-2015.

Pierini, S., and A. Rubino (2001), Modeling the Oceanic Circulation in the Area of the Strait of Sicily: The Remotely Forced Dynamics, *Journal of Physical Oceanography*, *31*, 1397–1412.

Placenti, F., K. Schroeder, A. Bonanno, S. Zgozi, M. Sprovieri, M. Borghini, P. Rumolo, G. Cerrati, S. Bonomo, S. Genovese, G. Basilone, D. Haddoud, B. Patti, A. El Turki, M. Hamza, and S. Mazzola (2013), Water masses and nutrient distribution in the Gulf of Syrte and between Sicily and Libya, *Journal of Marine Systems*, *121-122*, 36–46, doi:http://dx.doi.org/10.1016/j.jmarsys.2013.03.012.

Poulain, P.-M., and E. Zambianchi (2009), Surface circulation in the central Mediterranean Sea as deduced from Lagrangian drifters in the 1990s, *Continental Shelf Research*, *27*, 981–1001.

Richardson, D. (2006), Changes to the operational forecasting system, *ECMWF Newsletter*, *106*, 46pp.

Robinson, A., J. Sellschopp, A. Warn-Varnas, W. Leslie, C. Lozano, P. Haley, L. Anderson, and P. Lermusiaux (1999), The Atlantic Ionian Stream, *Journal of Marine Systems*, *20*, 129–156.

Roether, W., B. Klein, B. Manca, A. Theocharis, and A. Kioroglou (2007), Transient Eastern Mediterranean deep waters in response to the massive dense-water output of the Aegean Sea in the 1990s, *Progress in Oceanography*, *74*, 540–571.

Sammari, C., C. Millot, I. Taupier Letage, A. Stefani, and M. Brahim (1999), Hydrological characteristics in the Tunisia - Sardinia - Sicily area during spring 1995, *Deep Sea Research I*, *46*, 1671–1703.

Schroeder, K., A. Ribotti, M. Borghini, R. Sorgente, A. Perilli, and G.-P. Gasparini (2008), An extensive western Mediterranean deep water renewal between 2004 and 2006, *Geophysical Research Letters*, *4635(L18605)*.

Simmons, A. J., and J. K. Gibson (2000), *The ERAB-40 project plan, ECMWF ERA-40 Proj*, Rep. Ser. 1, European Center for Medium-Range Weather Forecasts, Reading, U. K.

Sorgente, R., A. Drago, and A. Ribotti (2003), Seasonal variability in the Central Mediterranean Sea circulation, *Annales Geophysicae*, *21*, 299–322.

Sorgente, R., A. Olita, P. Oddo, L. Fazioli, and A. Ribotti (2011), Numerical simulation and decomposition of kinetic energy in the Central Mediterranean: insight on mesoscale circulation and energy conversion, *Ocean Science*, *7*, 503–519, doi:10.5194/os-7-503-2011.

Stanev, E. V., and E. L. Peneva (2002), Regional sea level response to global climatic change: Black Sea examples, *Global and Planetary Changes*, *32*, 33–47.

Taupier-Letage, I. (2008), *On the Use of Thermal Images for Circulation Studies: Applications to the Eastern Mediterranean Basin*, Remote Sensing of the European Seas, Barale, V. and Gade, M. eds, Springer, Netherlands, doi:10.1007/978-1-4020-6772-3_12.

The-MEDAR-Group (2002), *Mediterranean and Black Sea Database of Temperature, Salinity and Biochemical parameters and Climatological Atlas*, Ifremer Ed., Plouzané, France, Available at http://www.ifremer.fr/sismer/program/medar/.

Tibshirani, R., G. Walther, and T. Hastie (2001), Estimating the number of clusters in a data set via the gap statistic, *Journal of the Royal Statistical Society, B.63(2)*, 411–423, doi:10.1111/1467-9868.00293.

Vetrano, A., G.-P. Gasparini, R. Molcard, and M. Astraldi (2004), Water flux estimates in the central Mediterranean Sea from an inverse box model, *Journal of Geophysical Research, 109(C01019)*, doi:10.1029/2003JC001903.

Zavatarelli, M., and G. Mellor (1995), A Numerical Study of the Mediterranean Sea Circulation, *Journal of Physical Oceanography, 25(6)*, 13841414.

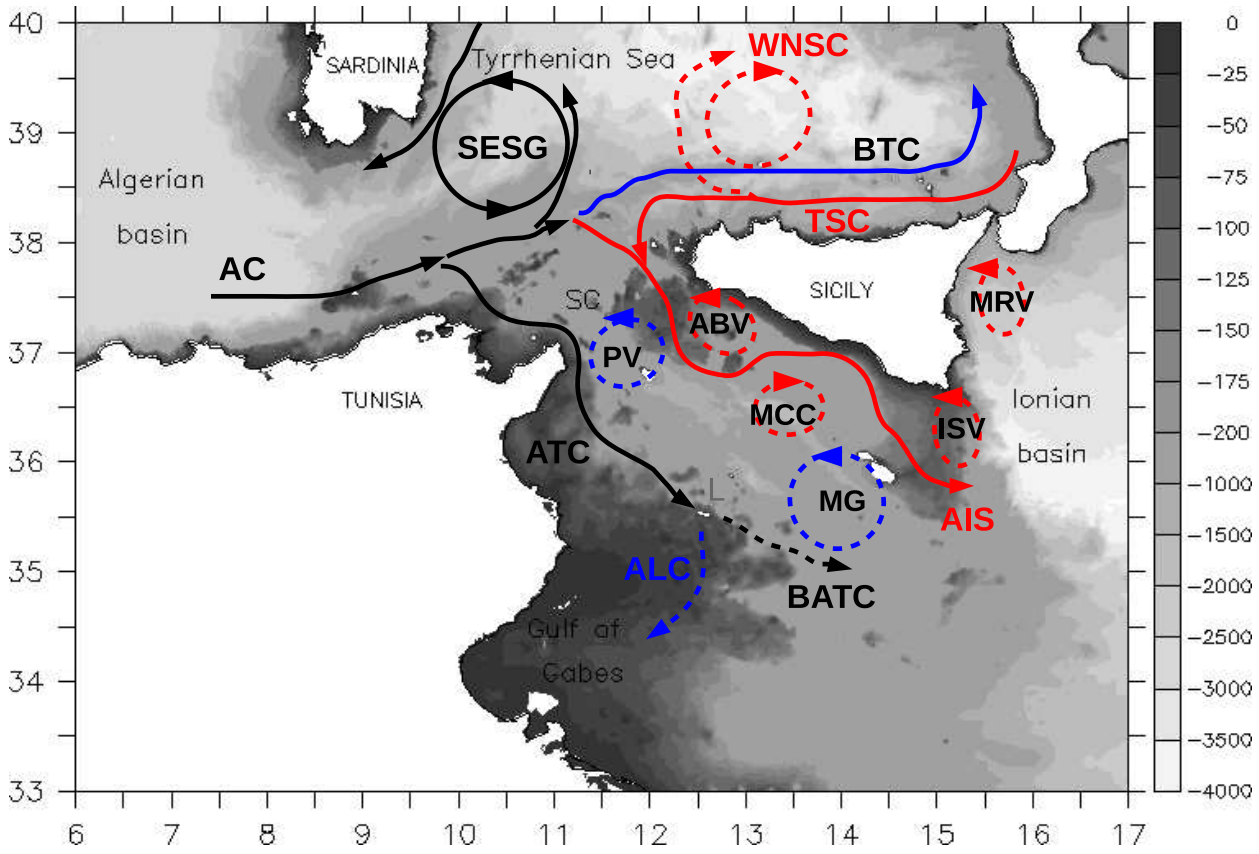

Figure 1. Scheme of the Atlantic Water circulation in the Sicily Channel (SC) area mainly summerized by *Sorgente et al.* [2011], with permanent patterns in *black* lines, summer patterns in *red* lines, and winter patterns in *blue* lines. Note that the Maltese Channel Crest (MCC) is drawn as an anti-cyclone (as in *Béranger et al.* [2004] and in *Lermusiaux and Robinson* [2001]). The new feature highlighted by this study, the Tyrrhenian Sicilian Current (TSC), is added in *red* because it is preferably simulated in summer. Corresponding acronyms are in Table 1. The bathymetry is drawn using a grey scale to highlight the shallow continental shelves in the Central Mediterranean (m). L is Lampedusa Island.

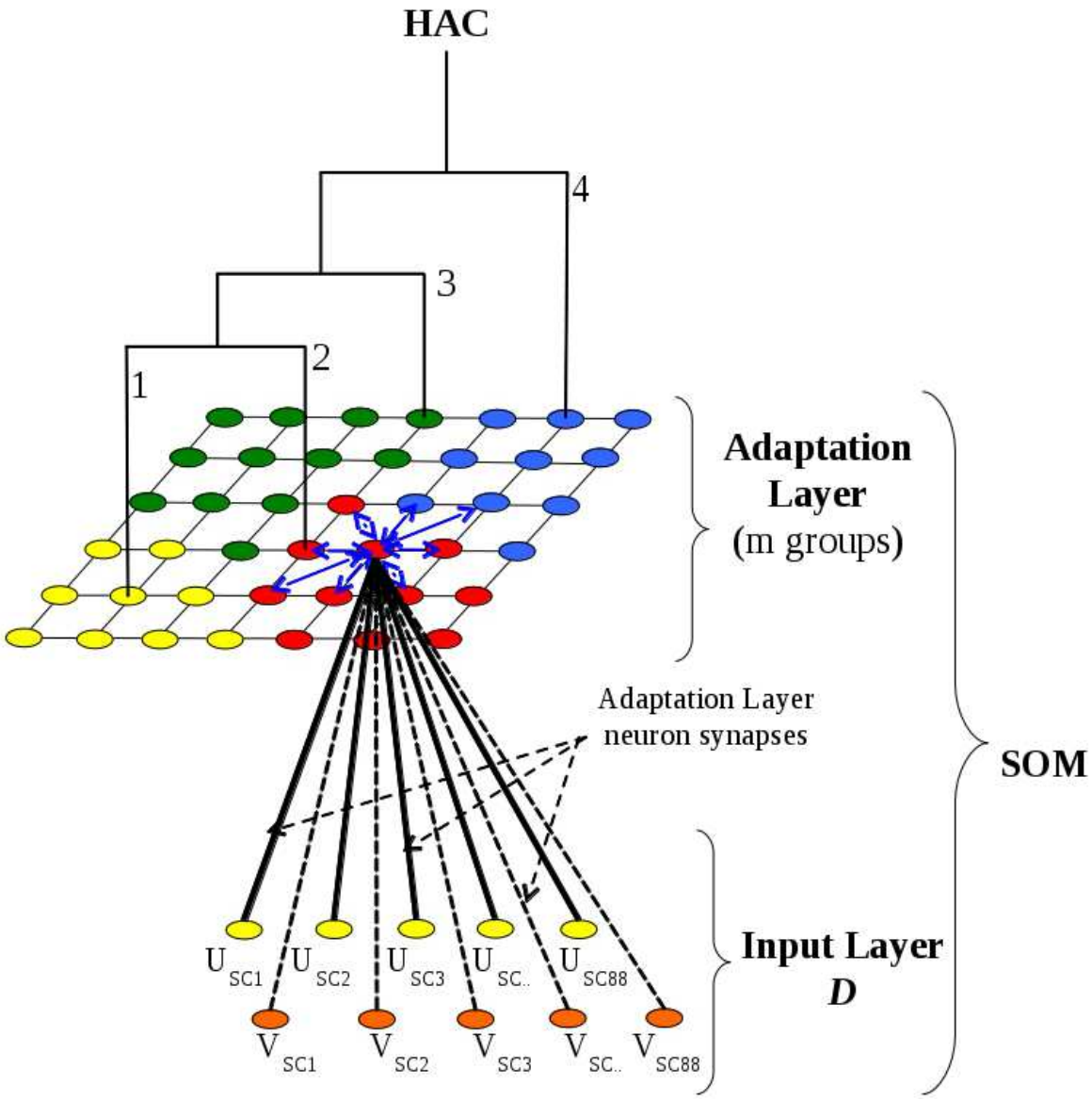

Figure 2. Schematic representation of the two steps of the clustering method $SOM + HAC$. (1) Structure of the self-organizing map (SOM): The network comprises two layers: an input layer used to present observations (88 current component daily values U_{SC} and V_{SC} at 30 m depth provided by the MED12 simulation covering the period 1966-2011) and an adaptation layer with 42 neurons (represented in colour). Each neuron is associated with a reference vector representing a set of U and V having close similarities representing a typical channel circulation. A neuron neighbourhood system is defined (schematized by the *blue* arrows) on the adaptation layer. (2) The 42 groups are clustered in 8 classes by the HAC algorithm, which is schematized by vertical sticks. For simplicity, only 4 classes are shown in the figure (*blue*, *red*, *green* and *yellow* neurons).

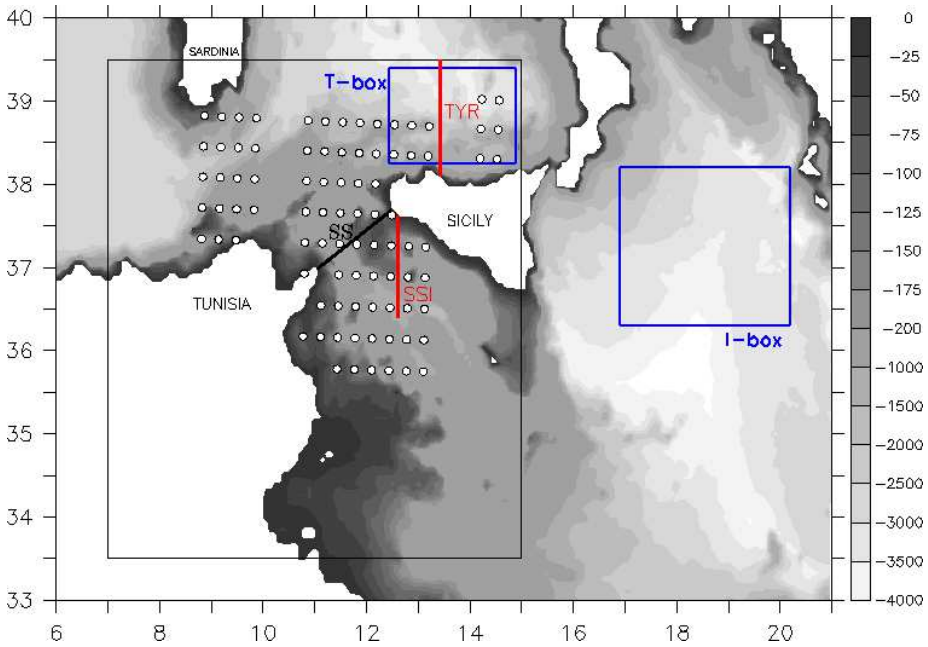

Figure 3. Definition of the SC sub-grid for application of the *SOM* method. The bathymetry of the MED12 model is drawn according to the *grey scale* given on the right-hand side of the figure. The *white* dots represent the 88 coordinates of the SC sub-grid composed of (176 values $= 2 \times 88$) the U and V components of the 30-m depth currents. This corresponds to a sub-grid increment of $\Delta x \approx 15$ km along the X axis in the W-E direction and to a sub-grid increment of $\Delta y \approx 25$ km along the Y axis in the N-S direction. The *black* line represents the area [33.5-39.5°N;7-15°E] covered by the maps of classes in Figures 5, 6 and 11. The *black* line between Tunisia and Sicily (SS) represents the SC section used for transport calculation reported in Table 3 and in Figures 9b and 10. The *red* lines (TYR) north and (SSI) south of Sicily represent the vertical sections in Figure 7. The 2 *blue* boxes, T-box in the Tyrrhenian Sea and I-box in the Ionian Basin, are used for calculation in Figure 15.

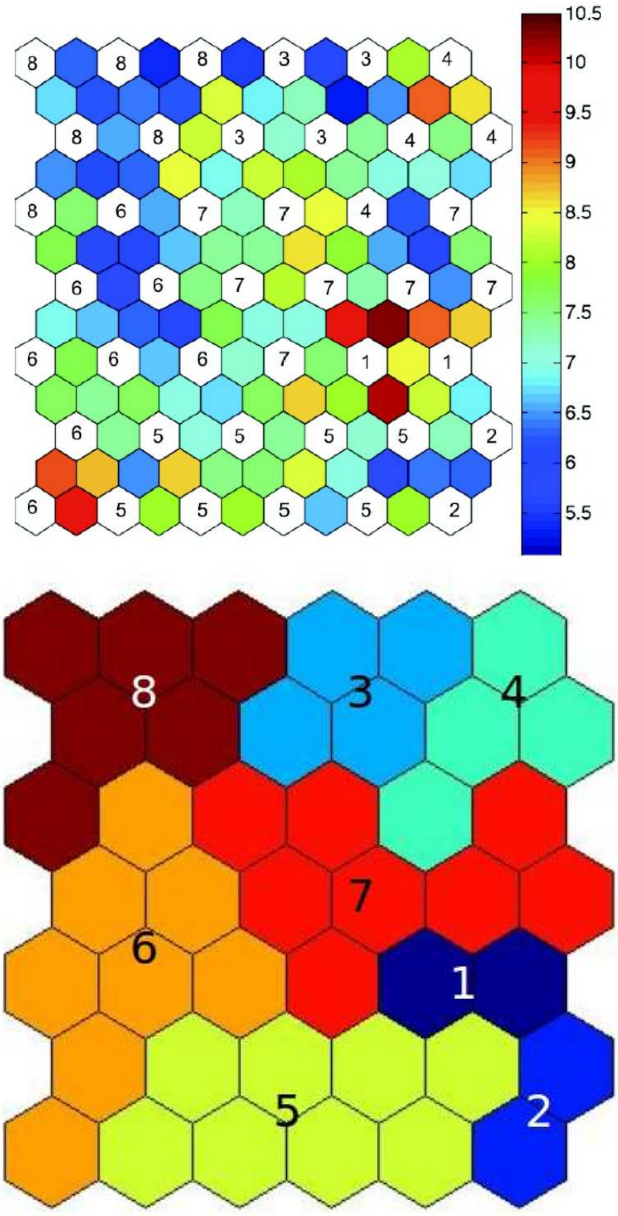

Figure 4. *(a: upper panel)* The topological map shows the distances between neurons (ranged from 5 to 10.5 according to the colour bar) and the corresponding classes. Each neuron is associated with a class. The classes are numbered from 1 to 8. *(b: bottom panel)* Neural map of the 8 classes obtained from the $SOM + HAC$ algorithm. The 8 classes are represented by different colours. The number of neuron is two for classes 1 and 2, four for classes 3 and 4, six for Class 8, and eight for classes 5, 6 and 7.

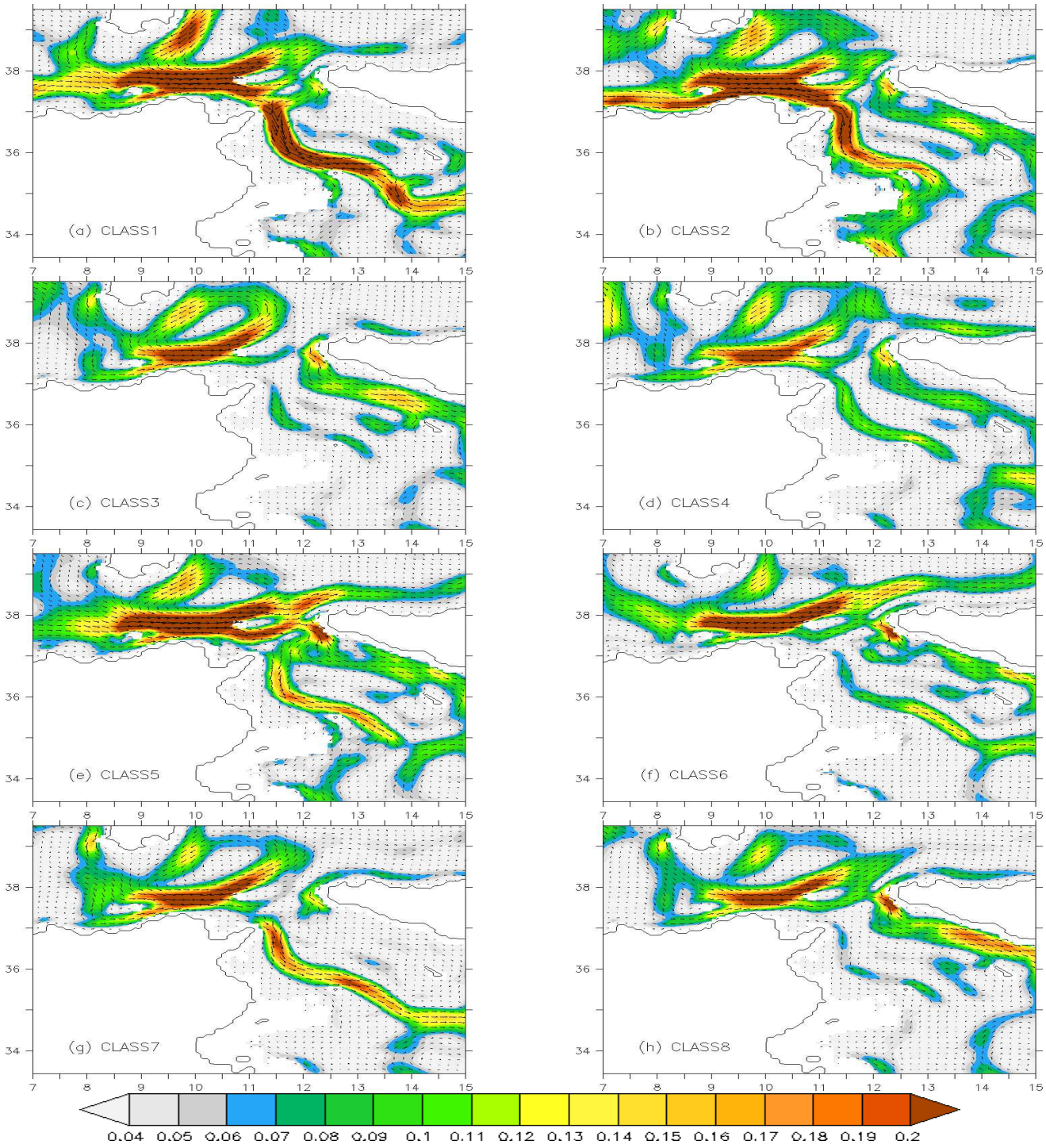

Figure 5. Maps of currents (modulus and vectors in m.s^{-1}) at 30-m depth for the 8 classes for the zoomed area indicated in Figure 3. Only one vector in every two is plotted.

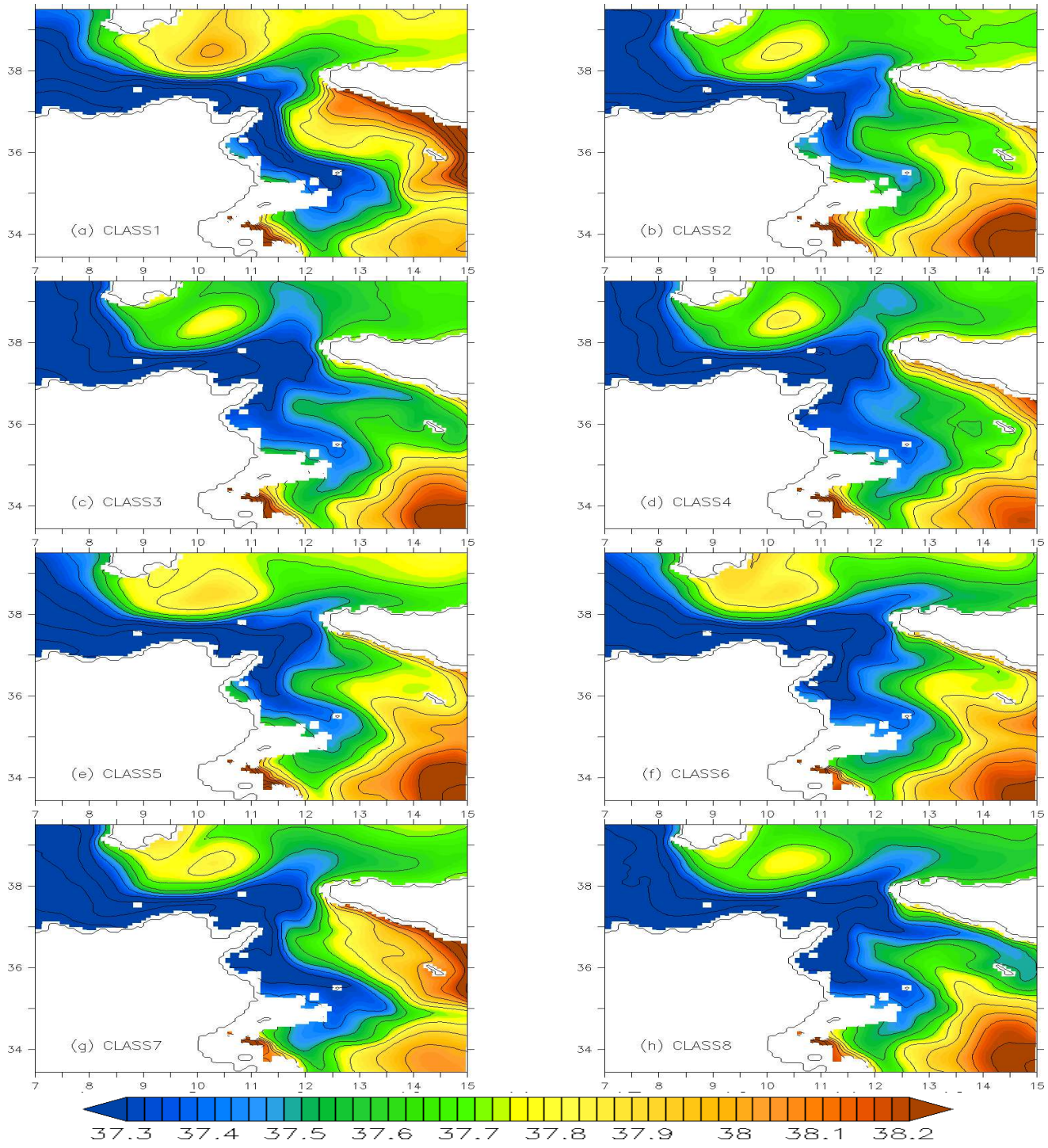

Figure 6. Maps of salinity at 30-m depth for the 8 classes of Figure 5 (contours every 0.1).

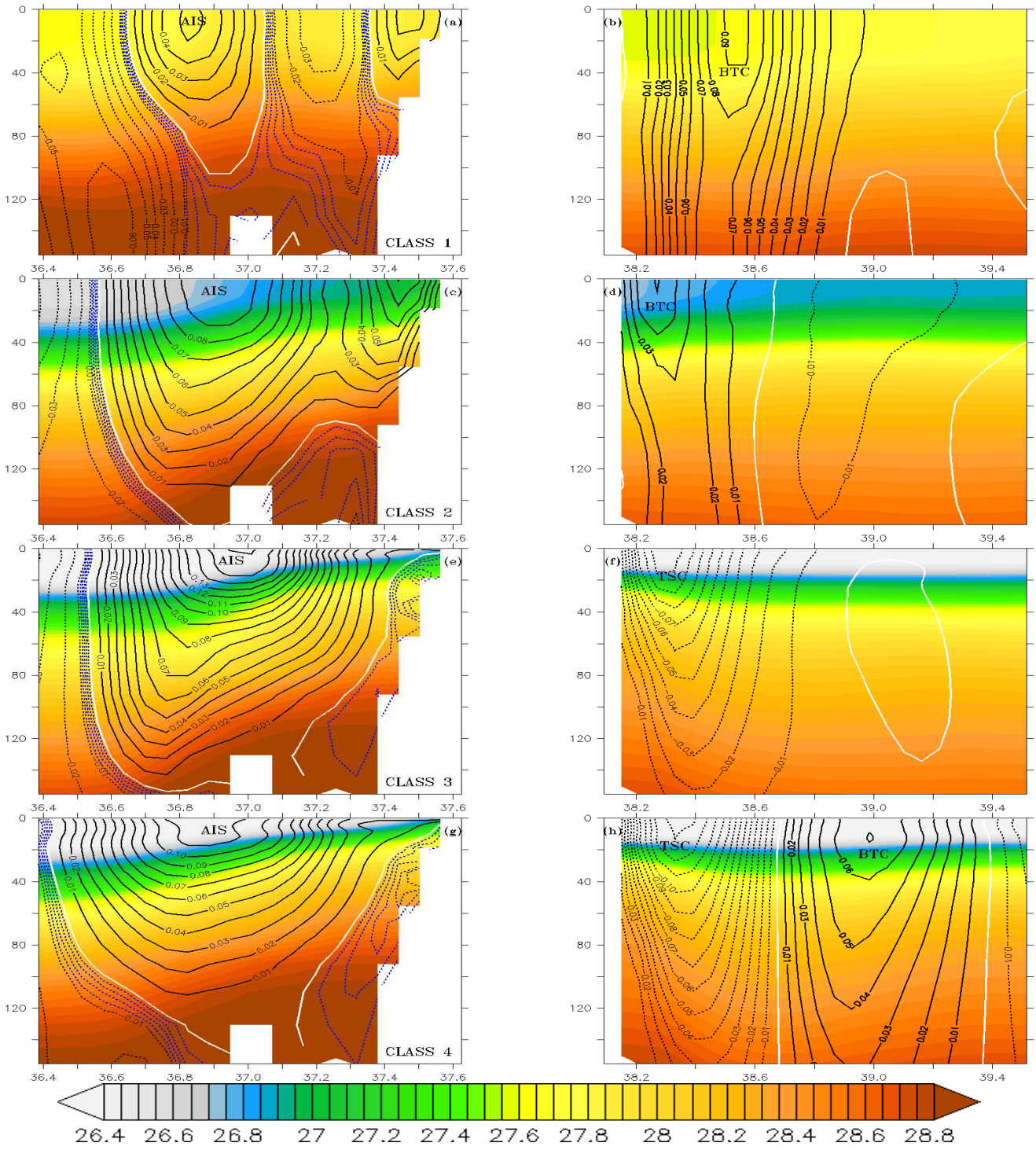

Figure 7. Vertical sections of density and currents along (left panels) south of Sicily (*red* line *SSI* in Figure3) and (right panels) north of Sicily (*red* line *TYR* in Figure 3), for the classes 1 to 4. The eastward velocities (positive values) are drawn in *full black* lines while the westward velocities are drawn in *dashed black* lines. *Black* contours are every 0.01 m.s^{-1} whereas the *white* line shows the zero velocity. In the left panels, *dashed blue* contours represent the westward velocities between -0.001 and -0.009 m.s^{-1} every 0.001 m.s^{-1}.

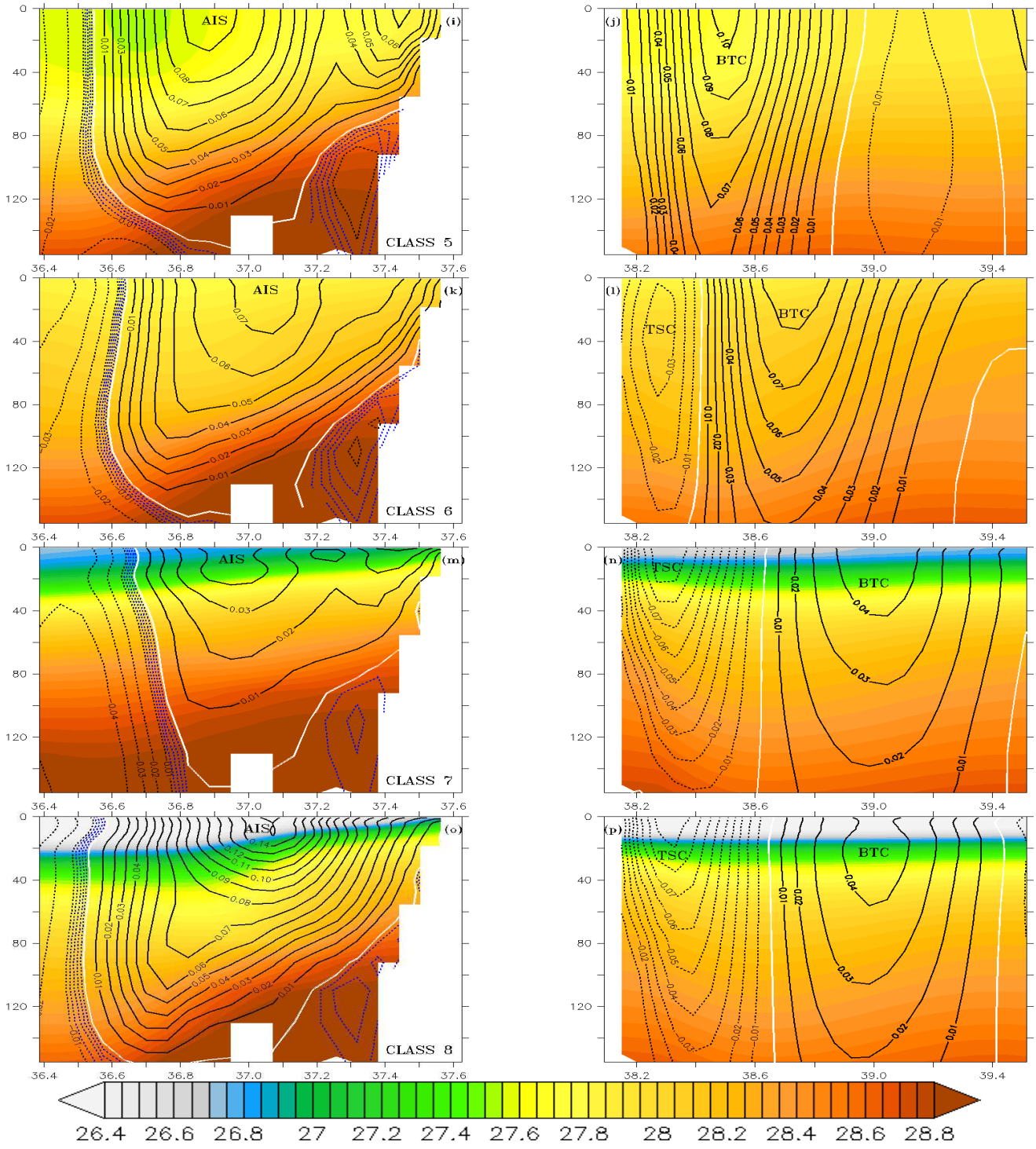

Figure 7 (continued). for the classes 5 to 8.

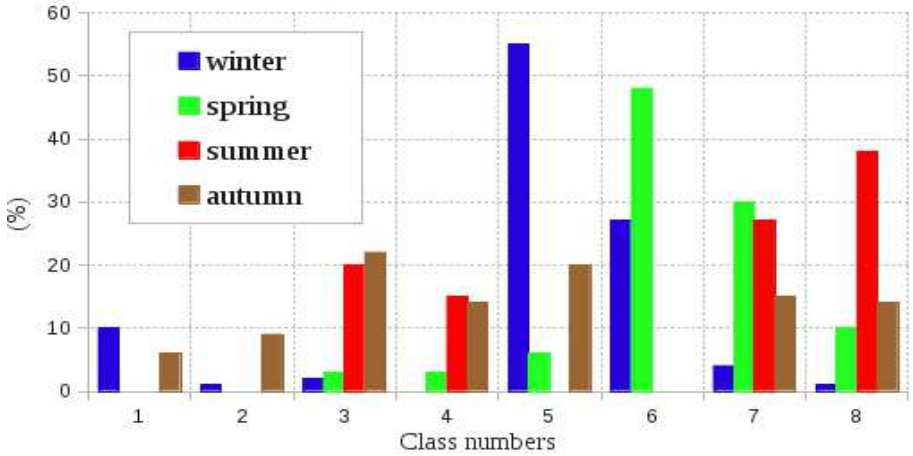

Figure 8. The x-axis represents the numbered classes, while the y-axis indicates the percent of seasonal occurrence of each class drawn in colors (DJF in *blue*, MAM in *green*, JJA in *red*, SON in *brown*) (for example, the sum of the DJF values is 100%).

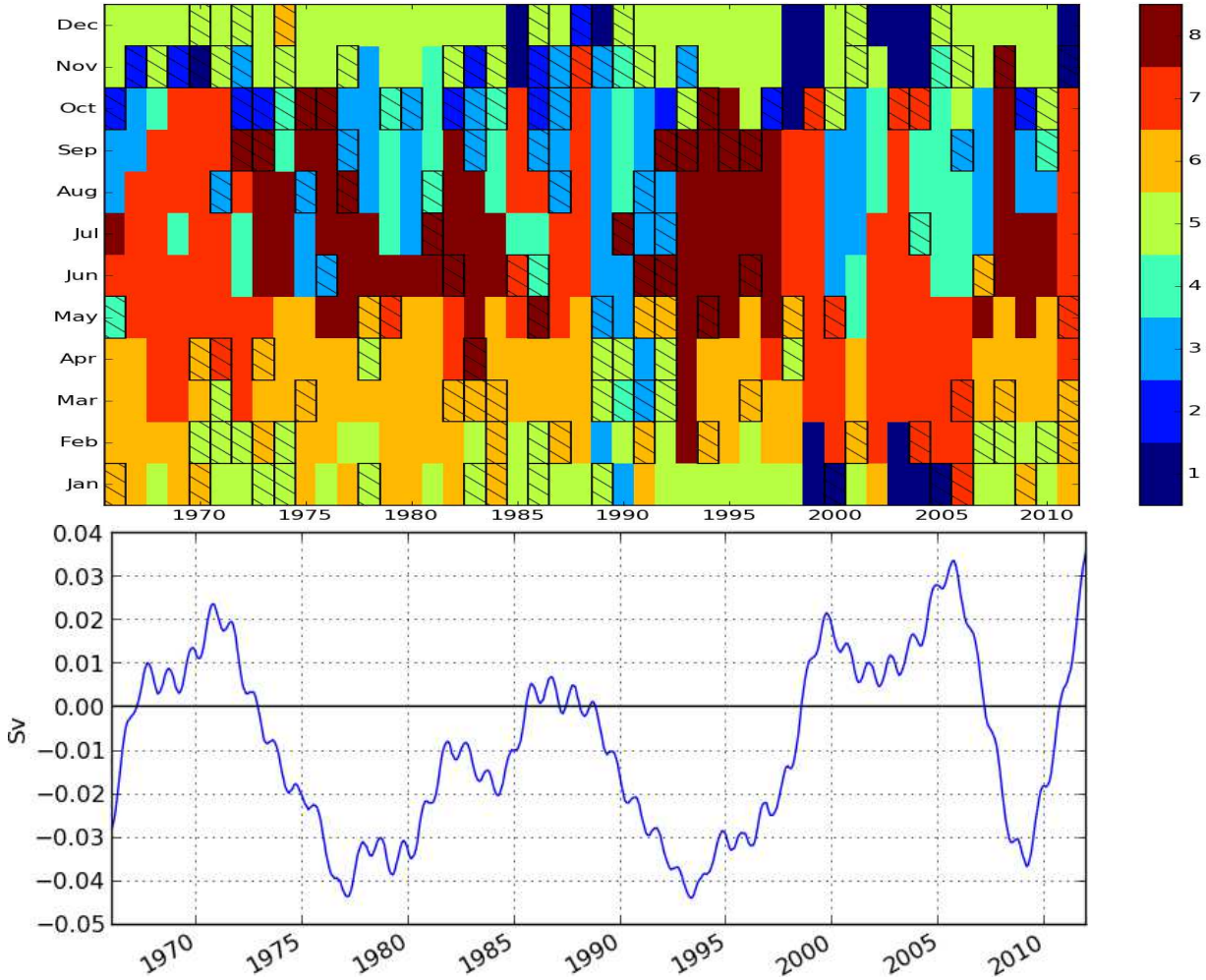

Figure 9. *(a: upper panel)* Time variability of the 8 classes: The x-axis represents the years from 1966 to 2011, while the y-axis indicates the months. The classes are identified by a color scale on the right of the figure. A month is affected to the class whose the daily class is the most frequently encountered during that month. The monthly confidence of that class is expressed as a percentage which is the number of occurrence days of the class with respect to the number of days in the month. Plain colors correspond to months whose class confidences are larger than 66%, striped color to months whose class confidences are between 66% and 33%. Most of the class confidences are larger than 66%, showing the efficiency of the classification. *(b: bottom panel)* Time-series of the monthly net transport through the SC, in sverdrups (Sv), from 1966 to 2011, filtered with a 3-year time-window (positive is eastwards).

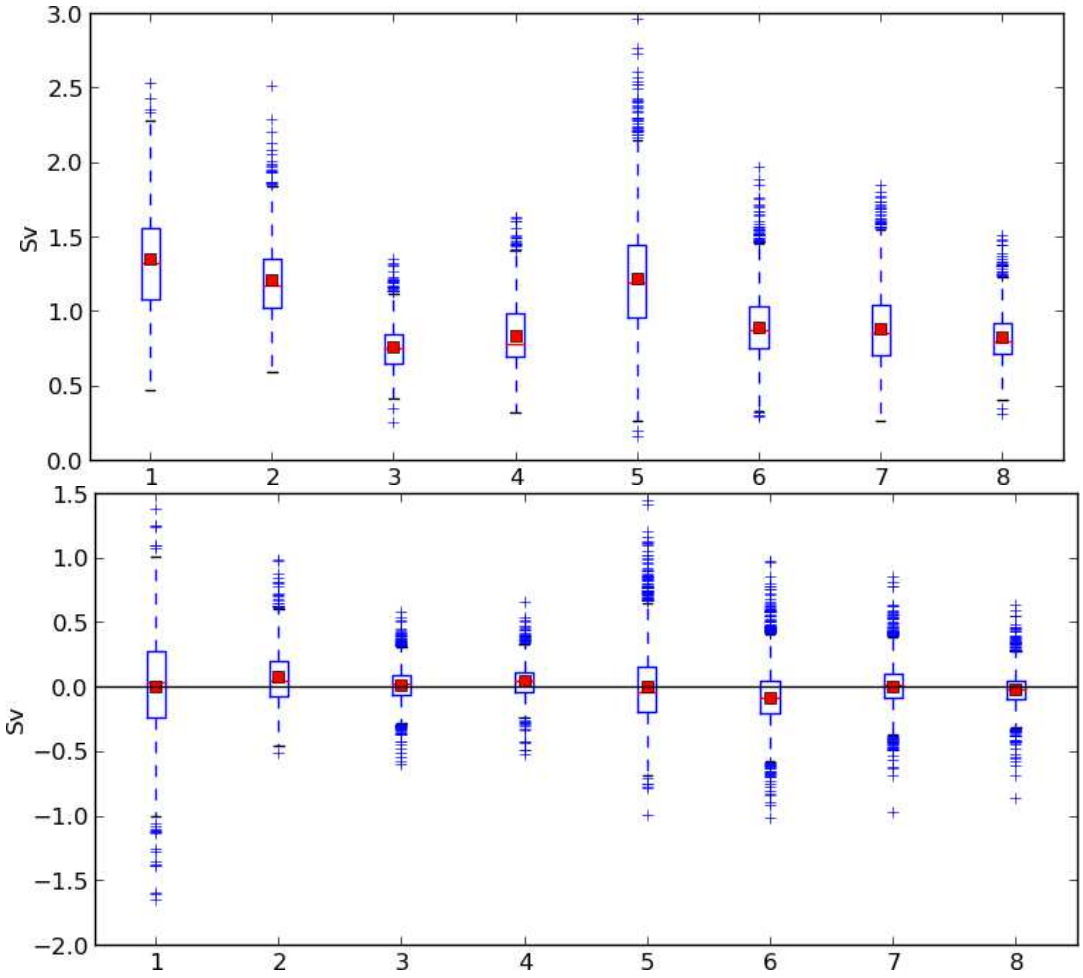

Figure 10. Box-and-whisker plots of the eastward *(a: upper panel)* and the net *(b: bottom panel)* transports (in sverdrups, Sv) through the SC for each class. The *blue* box extends from the lower to the upper quartile values, with a *red* line at the median and a *red* square at the mean. The end of the whiskers is 1.5 times the inter-quartile range past the first and third quartiles. Outliers are plotted as individual points.

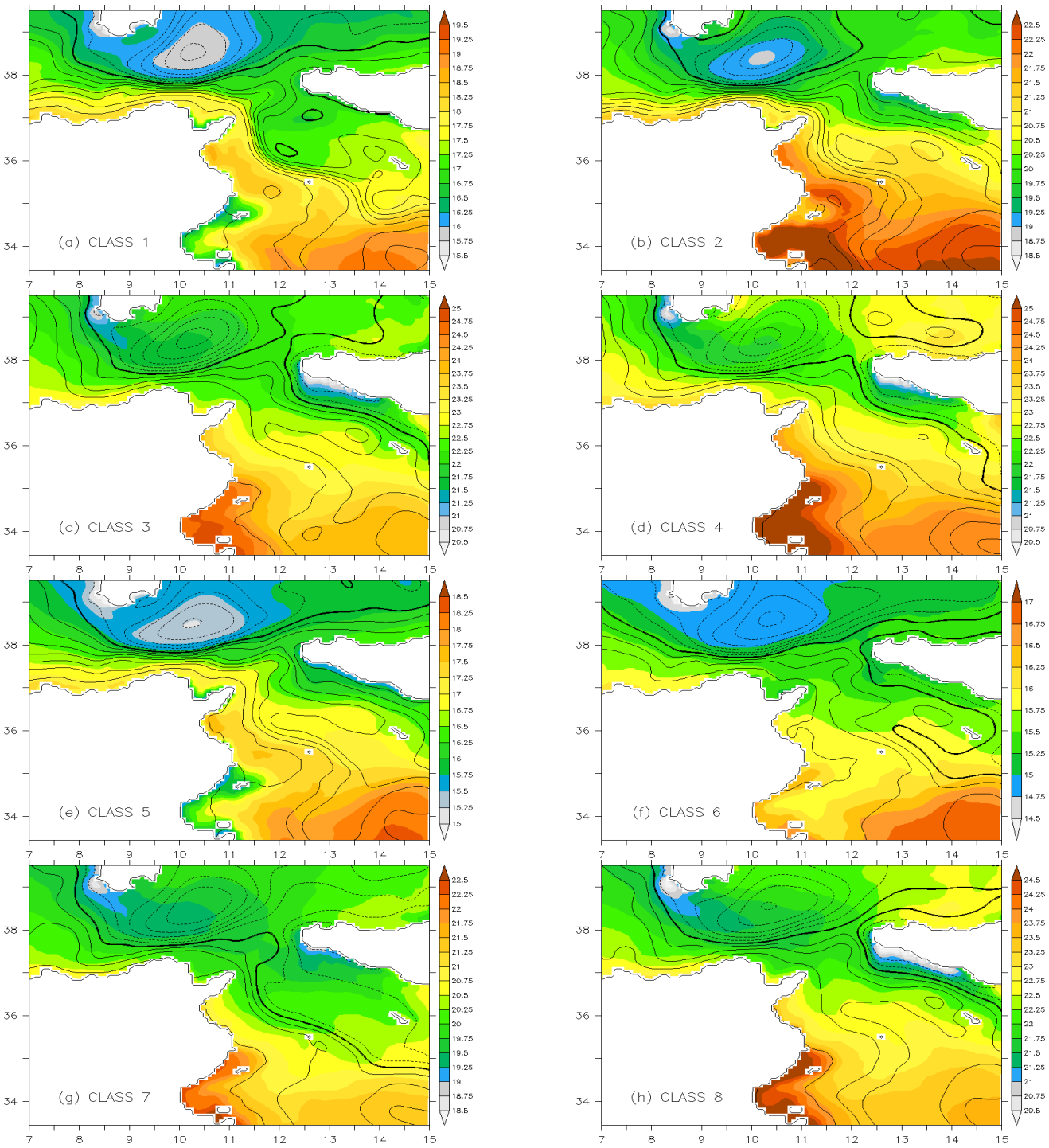

Figure 11. Sea-surface temperature (°C) for the 8 classes of Figure 5 and the associated sea-surface height anomaly represented at a contour interval of 0.02 m.s^{-1}.

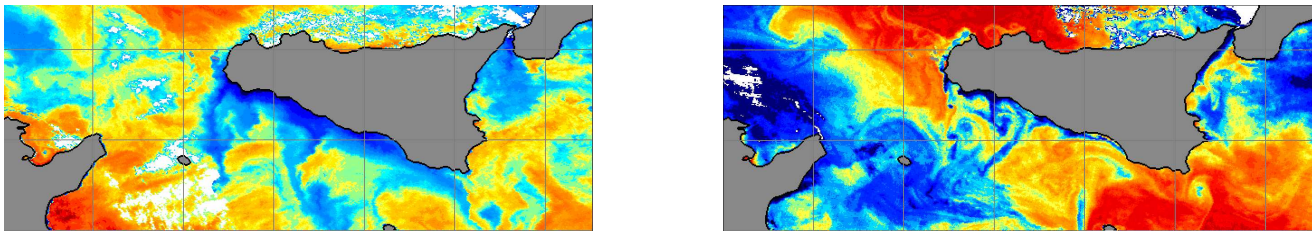

Figure 12. NOAA/AVHRR thermal images in 13 July 2005 *(a: left panel)* and in 22 July 2010 *(b: right panel)* Temperature increases from blue to red.

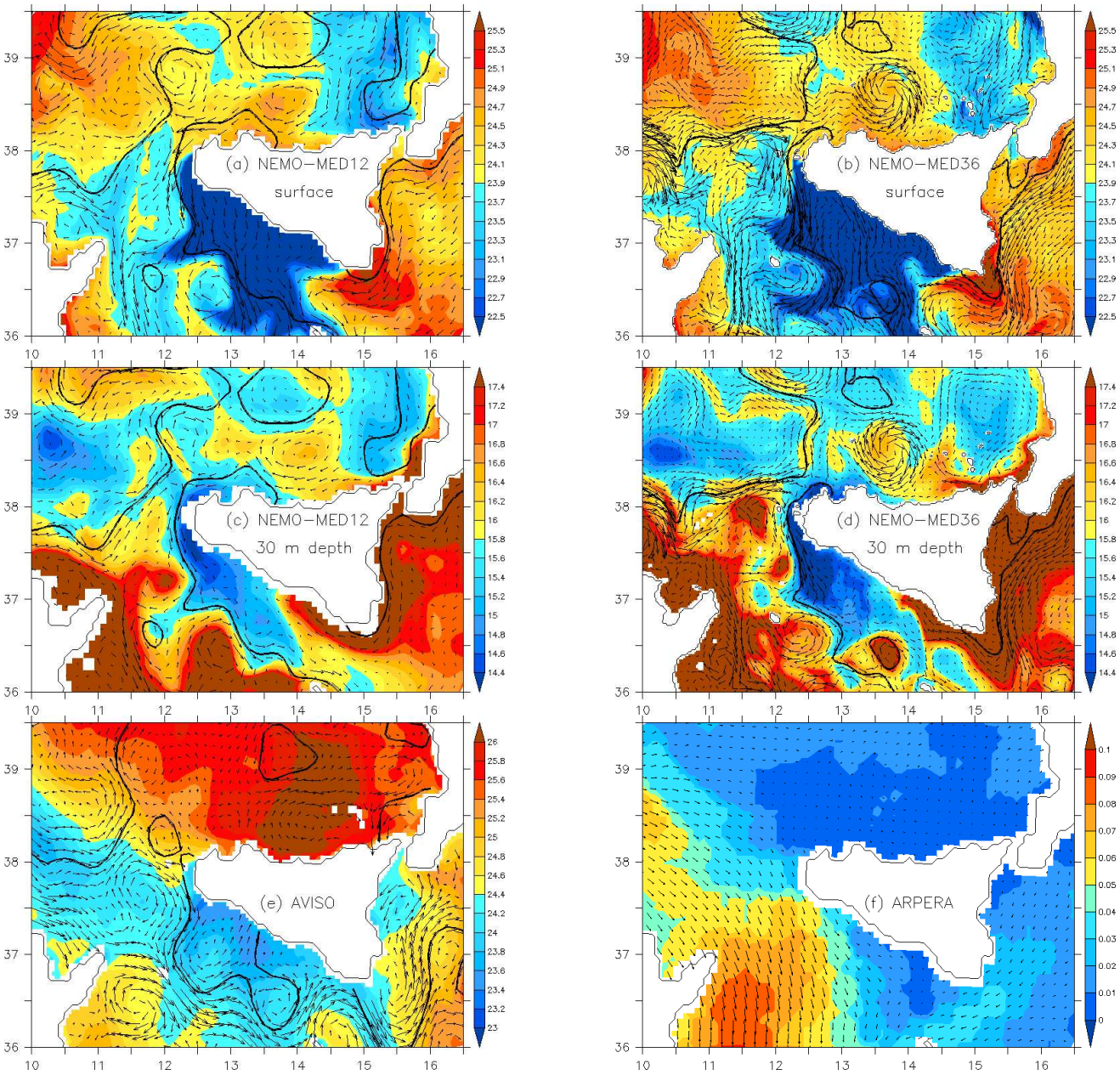

Figure 13. Snapshots of the sea-surface temperature (°C) and currents (m.s^{-1}) *(top panel)* and 30-m depth potential temperature and currents *(middle panel)* for MED12 (a, c) and MED36 (b, d) simulations forced by the same wind stress (N.m^{-2}) from ARPERA *(bottom panel, f)*. AVHRR sea-surface temperature from GOS [*Breivik et al.*, 2014] overplotted by the geostrophic currents and zero sea-surface height anomaly contour from AVISO [*CLS*, 2008] *(bottom panel, e)*. Note that the colourbar of the model sea-surface temperature is shifted by -0.5°C and the sea-surface height anomaly of the model is shifted by 0.085 m. All the ocean fields are from 15 July 2005, whereas the wind stress is from 11 July 2005. That wind, which is characterized by stress values lower than 0.05 N.m^{-2}, corresponds to the strongest winds occuring in the model during the 4-day period from 11 to 14 July 2005. Only one vector in every two is plotted in MED12 and ARPERA, and only one in every four in MED36.

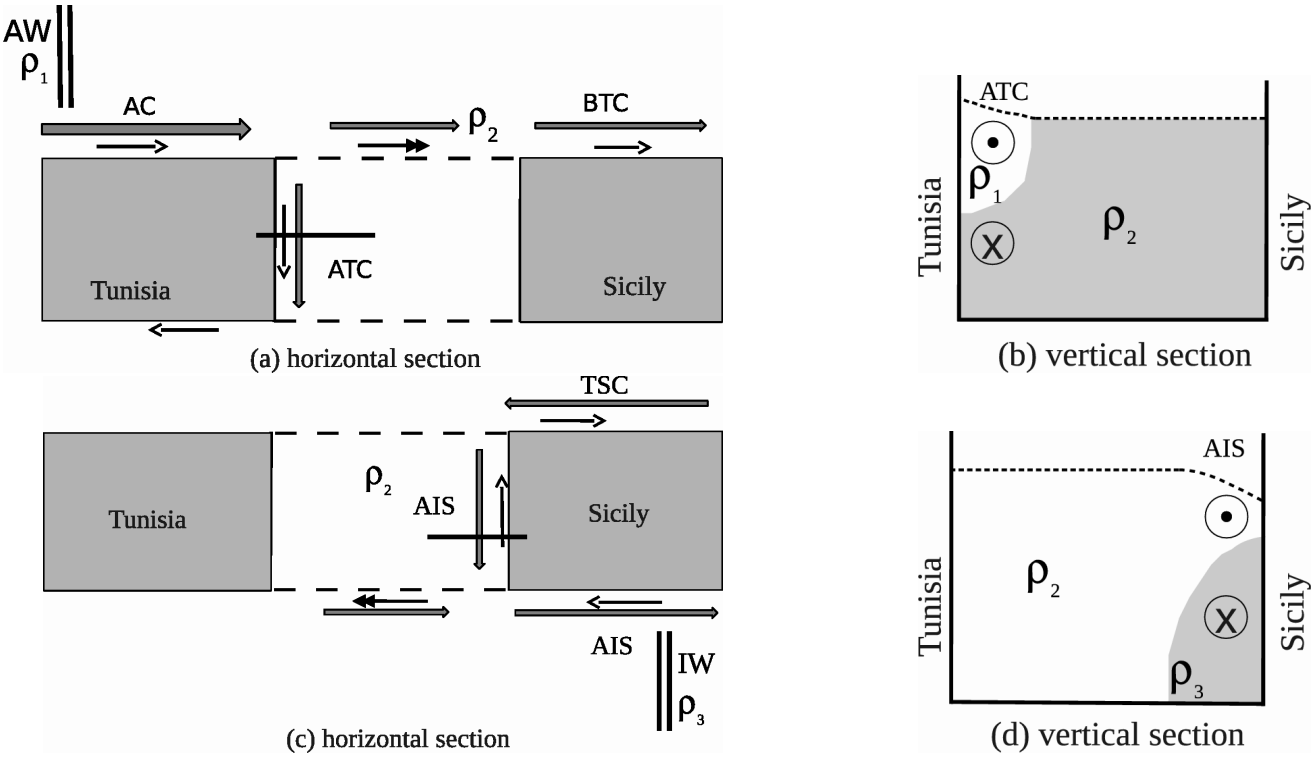

Figure 14. Schematic functioning of the surface currents in the Sicily Channel. The *thin black* arrows show the propagation of the Kelvin wave fronts. The double arrows show the double Kelvin wave. (a) and (c) represent horizontal sections of the Sicily Channel, the horizontal *black* segments represent the position of the vertical sections (b) and (d) crossing the channel. The two *upper panels* show a schematic formation of the ATC and BTC from the AC, according to *Herbaut et al.* [1998], (a) represents the surface currents (*thick grey* arrows) in the channel region. The vertical double line represents the water reservoir of AW (density $\rho_1 < \rho_2$) whose opening generates the Kelvin coastal jet. (b) represents a vertical section of the inflow of low-density water (in *white*) advected by the ATC into the channel over denser Eastern Mediterranean water (in *grey*). The two *lower panels* show a schematic explanation of the AIS and TSC formation following the mechanism suggested by *Molcard et al.* [2002]. (c) represents the surface currents (*thick grey* arrows) in the channel region. These currents are forced by the density gradient between the Tyrrhenian Sea and the Ionian Basin. Note that the surface currents flow in the opposite direction to that of the Kelvin wave front. The vertical double line represents the water reservoir of dense Eastern Mediterranean water (density $\rho_3 > \rho_2$) whose opening generates the Kelvin coastal jet. (d) shows the inflow of Eastern Mediterranean water (in *grey*) into the Tyrrhenian Sea which contributes to uplifting the water interface along the southern coast of Sicily, favouring the upwelling.

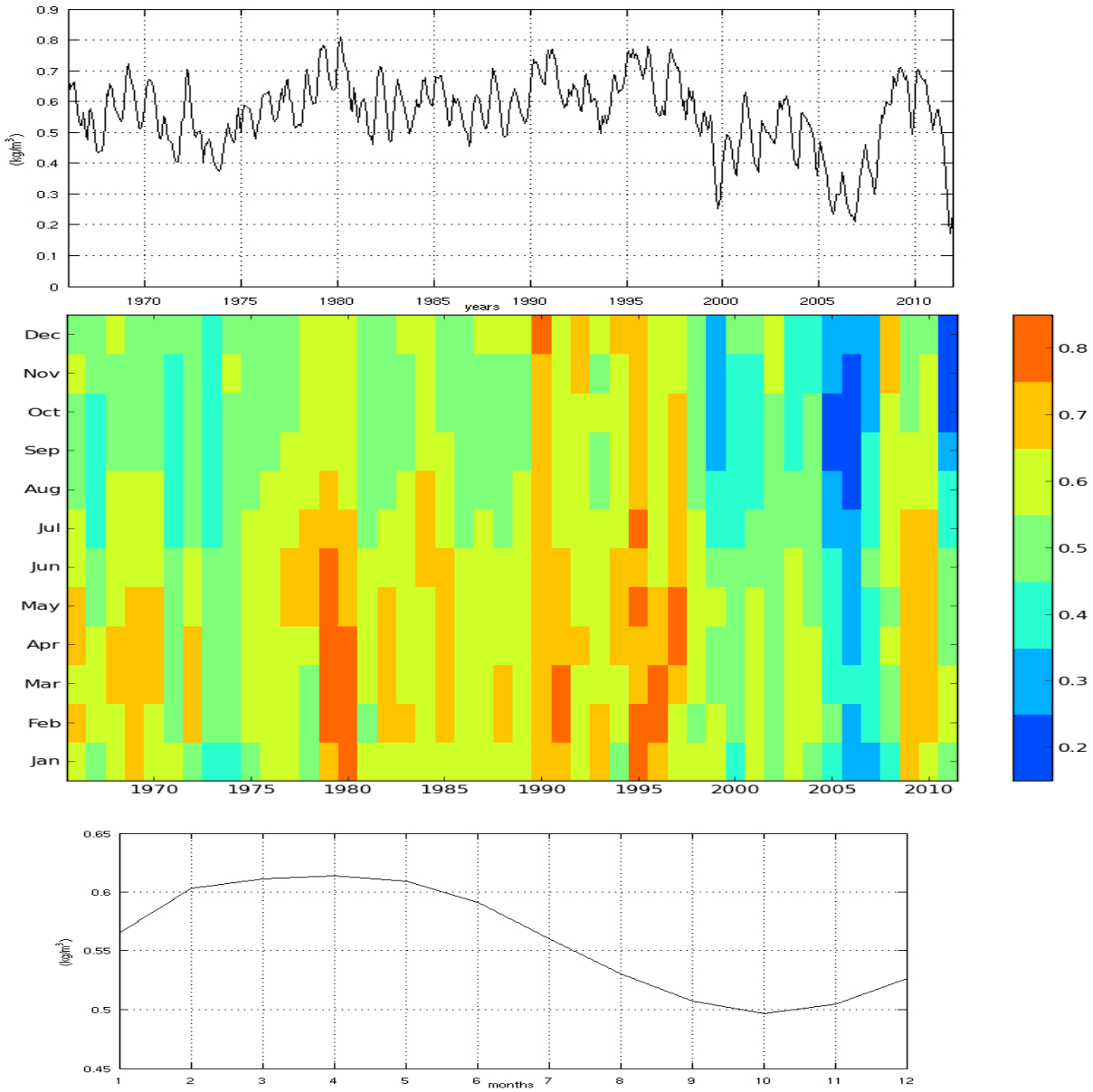

Figure 15. (a: upper panel) Time-series of the density gradient between the Ionian Basin and the Tyrrhenian Sea according to the monthly density differences calculated by averaging the Ionian and Tyrrhenian densities in two boxes (I-box and T-box, respectively, Figure 3) in the subsurface layer (50-150m). (b: middle panel) The *x-axis* represents the years from 1966 to 2011, while the *y-axis* indicates the months. The density differences of (a) ranged between 0.2 and 0.8 $kg.m^{-3}$ according to the given color scale on the right-hand side of the figure. (c: bottom panel) Climatological seasonal cycle of (a).

Acronym	Name	Notes
ABV	Adventure Bank Vortex	cyclonic
AC	Algerian Current	
AIS	Atlantic Ionian Stream	
ALC	Atlantic Libyan Current	
ATC	Atlantic Tunisian Current	
AW	Atlantic Water	
BATC	Bifurcation Atlantic Tunisian Current	
BTC	Bifurcation Tyrrhenian Current	
ISV	Ionian Shelf break Vortex	cyclonic
LIW	Levantine Intermediate Water	
MCC	Maltese Channel Crest	anti-cylonic
MG	Medina Gyre	cyclonic
MRV	Messina Rise Vortex	cyclonic
SESG	South Eastern Sardinia Gyre	cyclonic
TSC	Tyrrhenian Sicilian Current	
WNSC	Westward Northern Sicilian Current	
PV	Pantelleria Vortex	cyclonic

Table 1. Acronyms of Mediterranean oceanic features in the Sicily Channel.

Acronym	Name
ARPEGE-Climat	weather and forecating atmospheric model, CNRM
ARPERA	reanalysis-driven simulation made with ARPEGE, CNRM
AVHRR	Advanced Very High-Resolution Radiometer, US/NOAA
AVISO	Archiving, Validation and Interpretation of Satellite Oceanographic data, France
CNES	Centre National dEtudes Spatiales, France
CNRM	Centre National de Recherches Météorologiques, Météo-France, France
CNRS	Centre National de Recherche Scientifique, France
CMS	Centre de Météorologie Spatiale, Lannion, France
DGA	Direction Générale de l'Armement, Ministère de la Défense, France
ECMWF	European Centre for Medium-range and Weather Forecast
EEN	Energy and ENstrophy conservative
EOF	Empirical Orthogonal Functions
ERA	ECMWF Re-Analyses
GEBCO	General Bathymetric Chart of the Oceans
GENCI	Grand Equipement National de Calcul Intensif, France
GIS-Climat	Groupement d'Intérêt Scientifique Climat Environnement Société, France
GLORYS	oceanic re-analyses, Mercator Ocean, France
GMMC	Groupe Mission Mercator Coriolis, France
GOS	Gruppo di Oceanografia da Satellite
HAC	Hierarchical Ascendant Classification
HPC	High performance computer
HyMeX	Hydrological cycle in Mediterranean Experiment
IDRIS	Institut du Développement et des Ressources en Informatique Scientifique
INSU	Institut National des Sciences de l'Univers, CNRS
IPSL	Institut Pierre Simon Laplace, Paris, France
MEDAR	Mediterranean Data Archaeology and Rescue
MEDATLAS	Mediterranean and Black Sea climatological database
MED-CORDEX	Co-ordinated Regional Climate Downscaling Experiment
MORCE	Plateforme de MOdélisation Régionale CoupléE, IPSL
NEMO	Nucleus for European Modelling of the Ocean
NOAA	National Oceanic and Atmospheric Administration
SATMOS	Service d'Archivage et de Traitement Météorologique des Observations Spatiales (Météo-France-CNRS/INSU)
SiMED	Simulation de la circulation générale à mésoéchelle en MEDiterranée, GMMC
SOM	Self-organizing map
SST	Sea-surface temperature
TVD	Total Variance Dissipation

Table 2. Acronyms used in the text.

class number	1	2	3	4	5	6	7	8
median eastward transport (Sv)	1.347	1.214	0.758	0.836	1.221	0.894	0.881	0.824
mean eastward transport (Sv)	1.320	1.170	0.750	0.780	1.190	0.870	0.850	0.800
median net transport (Sv)	0.004	0.083	0.018	0.041	-0.003	-0.081	0.006	-0.022
mean net transport (Sv)	0.035	0.050	0.020	0.040	-0.040	-0.090	0.010	-0.020

Table 3. Values of the mean and median eastward and net transports (in sverdrups, Sv) through the SC for each class (see Figure 10).

month	1966	1967/ 1972	1973/ 1984	1985/ 1988	1989	1990/ 1997	1998/ 2000	2001	2002/ 2006	2007/ 2010	2011
Class 8	1	1	35	1	0	34	0	0	0	12	0
Class 7	1	34	4	15	0	1	16	0	29	0	7
transport	<0	>0	<0	>0	<0	<0	>0	>0	>0	<0	>0

Table 4. Number of months for each period for which classes 7 and 8 are present and the corresponding sign of the net eastward transport according to Figure 9.